Spatio-temporal variability of hyporheic exchange through a pool-riffle-pool sequence

Frank P. Gariglio[1], Daniele Tonina[1], Charles H. Luce[2]

[1] University of Idaho, Center for Ecohydraulics Research, College of Engineering, 322 E. Front St., Suite 340, Boise, ID 83702

[2] U.S. Forest Service, Department of Agriculture, Rocky Mountain Research Station, 322 E. Front St., Suite 401, Boise, ID 83702

Abstract

Stream water enters and exits the streambed sediment due to hyporheic fluxes, which stem primarily from the interaction between surface water hydraulics and streambed morphology. These fluxes sustain a rich ecotone, whose habitat quality depends on their direction and magnitude. The spatio-temporal variability of hyporheic fluxes is not well understood over several temporal scales and consequently, we studied their spatial and temporal variation over a pool-riffle-pool sequence at multiple locations from winter to summer. We instrumented a pool-riffle-pool sequence of Bear Valley Creek, an important salmonid spawning gravel-bed stream in central Idaho, with temperature monitoring probes recording at high temporal resolution (12-minute intervals). Using the thermal time series, weekly winter season seepage fluxes were calculated with a steady-state analytical solution and spring-summer fluxes with a new analytical solution that can also quantify the streambed thermal properties. Longitudinal pool-riffle-pool conceptualizations of downwelling and upwelling behavior were generally observed, except during the winter season when seepage fluxes tended towards downwelling conditions. Seepage fluxes near the edges of the channel were typically greater than fluxes near the center of the channel, and demonstrated greater seasonal variability. Results show that the interaction between streamflow and streambed topography has a primary control near the center of the channel whereas the interaction between stream water and groundwater table has a primary control on seepage fluxes near the banks of the stream.

Introduction

A substantial and growing literature on exchanges between groundwater and stream water argues that fine scale spatial variability in flows into and out of the streambed is important to aquatic biota [*Bruno et al.,* 2009; *Cooper,* 1965; *Malard et al.,* 2002; *Naiman,* 1998; *Stanford and Ward,* 1988; 1993; *Stuart,* 1953; *Tonina and Buffington,* 2009b], and may be important to reach scale nutrient and carbon cycling [*Kennedy et al.,* 2009a; *Marzadri et al.,* 2011; 2012; *Pinay et al.,* 2009; *Pretty et al.,* 2006; *Revsbech et al.,* 2005; *Storey et al.,* 2004; *Triska et al.,* 1989; *Zarnetske et al.,* 2011]. There is also a well-recognized notion that larger scale (1-10 km) contexts of stream setting may have fairly profound influences on local scale fluxes and their spatial variability [*Bencala et al.,* 2011; *Constantz et al.,* 2002; *Tonina and Buffington,* 2007; *Vannote et al.,* 1980]. While the profile view of hyporheic fluxes in the relatively short scale of a pool-riffle-pool (PRP) sequence (Figure 1) has been well studied [*Harvey and Bencala,* 1993; *Savant et al.,* 1987; *Tonina and Buffington,* 2009b], only limited empirical evidence has been applied to linking the fine scale flux heterogeneity exemplified by the PRP sequence in to the larger contexts of inter-meander connectivity and even valley slope variation [*Boano et al.,* 2010; *Wroblicky et al.,* 1998].

The seasonal contexts of changing flow and groundwater recharge add to the complexity of understanding cross-scale (sub-meter to km) interactions in groundwater-surface water exchanges [*Hannah et al.,* 2009]. For example at the local scale there is a change in the head gradients across riffle crests as stage varies in the stream, with more pronounced longitudinal hyporheic exchanges at lower flows [*Storey et al.,* 2003]. There is reason to expect that fine scale spatial patterns in hyporheic exchanges will shift as the larger scale contexts shift over time as well. While there are some streams that may be ‘losing’ and ‘gaining’ throughout the year, it is probably more common for reaches to oscillate between net gain and net loss as seasons change from a wet season (or melt season) and a dry season [e.g. *Whiting and Pomeranets,* 1997]. Because many aquatic biota use hyporheic habitats for only a portion of their life cycle, these seasonal shifts in context may hold important clues about habitat preferences that would not be evident if dynamic fluxes were not considered [*Baxter et al.,* 2003; *Geist and Dauble,* 1998; *Malcolm et al.,* 2003; *Van Grinsven et al.,* 2012]. The temporal context is also an important link between reach scale hyporheic fluxes and runoff generation throughout the watershed, particularly in snowmelt driven watersheds, where local groundwater recharge and streamflow are likely to be asynchronous. Because temperature, nutrient, and carbon inputs vary seasonally as well, additional insights about temporally varying spatial patterns in hyporheic exchange may be important for work in these areas [*Kennedy et al.,* 2009b; *Lautz,* 2012; *Marzadri et al.,* 2012; 2013; *Tonina and Buffington,* 2011].

Consequently in this paper, we analyze the spatio-temporal variability of the upwelling and downwelling fluxes along a pool-riffle-pool sequence at multiple depths within the streambed sediment and at multiple longitudinal and transverse locations. We also investigate the seepage fluxes at the water-sediment interface in connection with the surrounding groundwater. To address these goals we use a set of measurements along and across a PRP sequence in a reach of a meandering stream that is somewhat orthogonal to the valley slope. The stream is in high mountains with a pronounced winter low flow and spring high flows. Measurements were taken over a 10 month period starting in the low flow fall season and progressing through the recession limb the following summer. The multi-season timescale provided additional challenges in data collection and analysis, most obviously in limiting choices for measurement. All flux estimates are based on temperature as a tracer, with a steady state solution for winter when there is no diurnal variation in water temperatures [*Bredehoeft and Papadopulos,* 1965], and a solution based on diurnal temperature variations for the spring and summer seasons [*Luce et al.,* 2013]. Because fluxes in some periods and locations were very small, and the direction of flux is important to ecological interpretations, we modified the diurnal temperature variation solution from the traditional amplitude and phase solutions [*Goto et al.,* 2005; *Hatch et al.,* 2006; *Keery et al.,* 2007; *Stallman,* 1965] to use an amplitude-phase combination approach detailed in *Luce et al.* [2013], which is briefly reviewed herein for the reader. This second method also provided information on the thermal diffusivity parameter, which improves estimates from the steady-state approach in winter as well. Although the measurements are along just one reach, the contextual setting of that reach, the lateral distribution of measurements, and the strong contrasts in seasonal hydrology provide insights about the interaction of that reach with valley scale groundwater-surface water exchanges.

Study Site, Discharge Measurements and Instrumentation

Study Site

Bear Valley Creek is a 4th order [*Strahler,* 1952] mountain stream in central Idaho and is a tributary to the Middle Fork of the Salmon River (Figure 2). The watershed area upstream of the study site is approximately 161 km^2. The minimum elevation is approximately 1966 m near the watershed outlet and the maximum watershed elevation is approximately 2660 m. The basin hydrology is snowmelt dominated. Much of the precipitation occurs as snow during the winter months, with yearly precipitation averaging approximately 767 mm. The spring snowmelt period (late April – early June) produces the largest discharges in the stream. Bankfull flow is estimated at approximately 7.0 m^3 s^{-1} [*McKean and Tonina,* 2013]. The receding limb of the hydrograph extends into the summer and fall seasons. Late fall (September – October) experiences the lowest discharges, with low flows typically averaging approximately 0.8 – 1.3 m^3 s^{-1}.

The average channel width is approximately 15 m. The slope of the stream channel is approximately 0.0035 m m^{-1}. Bear Valley Creek supports an extensive meadow system and is a sinuous channel, having a sinuosity index of 1.5 (values for natural streams range between 1 [straight] and approximately 4 [greatly meandering]). In the vicinity of the study site, Bear Valley Creek flows through an unconfined alluvial valley. The overall valley slope is approximately 0.0055 m m^{-1} and is approximately 1.6 times larger than the longitudinal stream gradient. The stream is classified as a pool-riffle reach based on the *Montgomery and Buffington* [1997] classification. Overbank flows are common during spring runoff and result in inundation of the extensive floodplain for a portion of the year. Off channel ponding resulting from these flows, and seasonally extended by beaver dam construction and paleo-channels, adds heterogeneity and complexity to HZ habitats. The system is used extensively by Chinook salmon (*Oncorhynchus tshawytscha*) and steelhead trout (*Oncorhynchus mykiss*) for both spawning and rearing life stages. The streambed consists of clean gravels (D_{50} = 35 mm) that are highly suited for construction of salmonids egg nests, commonly referred to as redds [*Tonina and Buffington,* 2009b]. The pool-riffle-pool morphology, low input of fine sediments, clean gravel substrate and stable bed features result in conditions that promote HZ seepage fluxes along much of the stream.

Discharge, Precipitation, Air Temperature Measurements

Due to the remote nature of the site and seasonal accessibility constraints, precise measurements of discharge, precipitation and air temperature are not available at the study site. While discharge is not measured at the study site an area-partitioned flow reconstruction can be conducted using the US Geological Survey (USGS) gage 13309000 (Bear Valley Creek near Cape Horn, Idaho), which is located approximately 12 km downstream of the study site. The period of record for the Bear Valley Creek gage (13309000) includes summer daily discharge measurements from 1921 through 1928 and continuous daily discharge measurements from WY 1929 through WY 1960.

Due to the incomplete period of record for gage 13309000, an additional USGS gage 13295000 (Valley Creek at Stanley, Idaho) can be used to reconstruct missing discharges at USGS gage 13309000 based on the reliable scaling ratio of the two gages (obtained during periods of complete data for both gages). The period of record for the Valley Creek gage (13295000) includes daily discharge measurements from 01 June 1911 through 31 October 1913, 01 May 1921 through 07 December 1971, 24 April 1972 through 30 September 1972 and WY 1993 through WY 2010. Although precise discharge at the study site is not measured during the time period of interest, the overall characteristics of the hydrograph (timing of peak and low flows, storm response, rising and falling limb characteristics, etc) based on the reconstruction can be used to infer general flow conditions with discharge errors below 16% [*McKean and Tonina,* 2013].

Instrumentation

Surface water and streambed temperatures were monitored at nine locations spanning a PRP morphological feature in Bear Valley Creek. Five temperature monitoring probes were installed along the PRP sequence near the center of the channel to measure representative longitudinal locations (downstream end of pool, riffle head, riffle crest, riffle tail, and upstream end of the next pool). In addition to the five probes installed along the PRP sequence, four probes were installed in the transverse direction across the channel. These probes were installed at the end of the upstream pool and across the riffle crest. Figure 2 shows the spatial arrangement and location codes for each temperature monitoring location.

Each temperature monitoring probe housed four discrete temperature sensors. Temperatures were measured with the Onset StowAway TidBiT temperature sensors. The manufacturer reported measurement range for the temperature sensors is -4°C to 38°C with a resolution of

0.15°C and an accuracy of 0.1°C. The upper three sensors were installed at a spacing of 10 cm, with a fourth temperature sensor installed 30 cm below the third sensor. Sensors were nested inside of a 2.5-cm SDR 21 cold water PVC pipe. The PVC pipe was perforated at each sensor location to allow direct contact with streambed sediments and seepage water. Styrofoam material was inserted in between sensors to prevent any preferential flowpaths from developing vertically inside of the PVC pipe.

Probes were located in the streambed sediment in pilot holes created by pounding a rod into the streambed and then removing the rod and inserting the probe in its place. This allowed positioning the topmost sensor flush with the surface water-streambed interface. Temperature measurement depths were 0, 10, 20 and 50 cm. After installation, the location of each probe was surveyed with a research grade robotic total station (Leica TPS 1000), whose position was previously geo-referenced. The actual position of the topmost sensor relative to the streambed was recorded and the vertical location of each sensor was then corrected. Note that the distance between sensors did not change because they were housed in the PVC pipe but only the probe set was translated vertically. Sensors recorded streambed temperature every 12 minutes. Data collection began on 16 October 2006 and ended on 11 July 2007 (265 days).

Temperature sensors were checked prior to and following deployment for temporal or thermal drift. No drift was detected for any of the sensors and therefore no corrections were applied. Thermal profiles were visually examined to determine if preferential vertical flow was occurring at any of the sensor locations due to disruption of the streambed sediments during installation. It was determined that preferential vertical flow was likely occurring for several sensor locations immediately after installation, but that settling of streambed sediments soon established flowpaths more representative of the streambed HZ. No temperature measurements were used for the first 45 days (initially due to visually observed preferential flow paths and subsequently due to flow patterns that were transitional from diurnally fluctuating temperatures to steady-state winter conditions) so it is not expected that strong preferential flowpaths remained at the beginning of the thermal analyses.

Methods

The governing equation for the one-dimensional advection-diffusion equation can be expressed as [*Bredehoeft and Papadopulos,* 1965; *Goto et al.,* 2005; *Hatch et al.,* 2006; *Keery et al.,* 2007; *Lapham,* 1989; *Marzadri et al.,* 2013; *Stallman,* 1965]:

$$\frac{\partial T}{\partial t} = \kappa_e \frac{\partial^2 T}{\partial z^2} - \frac{q}{\gamma}\frac{\partial T}{\partial z} \quad (1)$$

where T is temperature (°C), t is time (s), κ_e is the effective thermal diffusivity ($m^2\ s^{-1}$), z is depth into the streambed (m) (note that z is defined as positive downward), q is the Darcy flux ($m\ s^{-1}$). The Darcian flux, q, is related to the pore water velocity, u, by $u = q/n$, where n is the sediment porosity (-; assumed to be 0.30 for this study); q is also related to the thermal front velocity, v_t, by $v_t = q/\gamma$ where $\gamma = \rho c/\rho_f c_f$ and ρc is the heat capacity of the sediment-water matrix (2.720 x 10^6 J m^{-3} °C^{-1}) while $\rho_f c_f$ is the heat capacity of water (4.186 x 10^6 J m^{-3} °C^{-1}). Thermal dispersivity (β) was assumed to be negligible. Solutions used during the winter and spring/summer seasons differ in the boundary conditions and assumptions used to solve equation (1).

Winter Seepage Flux

The solution to equation (1) presented by *Bredehoeft and Papadopulos* [1965] assumes steady state thermal conditions within the streambed ($\partial T/\partial t \rightarrow 0$). The upper boundary corresponds to the interface of the surface water and the streambed (z = 0) while the lower boundary corresponds to the lowermost temperature measurement location ($z = L$, where L is the total length of the measured sediment zone, or 50 cm for our application). Boundary conditions at these locations can be summarized as [*Bredehoeft and Papadopulos,* 1965]:

$$T_z = T_0 \; at \; z = 0 \tag{2}$$

$$T_z = T_L \; at \; z = L \tag{3}$$

where T_z is the temperature (°C) at any depth, z, T_0 is the temperature at the upper boundary (°C) and T_L is the lowermost temperature measurement (°C). The solution to equation (1) with boundary conditions (2) and (3) is:

$$\frac{(T_z - T_0)}{(T_L - T_0)} = \frac{\exp\left(\frac{\psi z}{L} - 1\right)}{[\exp(\psi) - 1]} \tag{4}$$

where $\psi = c_f \rho_f qL / \lambda_0$. The dimensionless parameter, ψ, is positive when q is positive (i.e. downward flow) and negative when q is negative (i.e. upward flow) and λ_0 is the thermal conductivity of the sediment-fluid matrix (W m^{-1} °C^{-1}).

Weekly average temperatures for each monitoring location and depth were calculated from 10 December 2006 through 10 March 2007. Temperatures during this period were visually determined to approximate thermally steady state conditions (see Figure 4). To further refine acceptable temperatures used for flux calculations, if the total range in observed temperatures during the week was less than 0.6 °C (±0.3 °C, which is three times the sensor accuracy and allows for slight differences due to sensor precision) then conditions were treated as steady state. The Solver add-in for Microsoft Excel was used to solve equation (4) following the method presented by *Arriaga and Leap* [2006]. The lower limit of accepted velocities was taken as [*Bredehoeft and Papadopulos,* 1965]:

$$|q| = \frac{0.5\lambda_0}{c_f \rho_f L} \tag{5}$$

Velocities with a magnitude less than that predicted from equation (5) are not reported. For non-unique solutions, which occurred when temperatures did not provide any gradient within the upper three sensors such that a unique downwelling or upwelling flux could be determined, the smallest possible seepage flux to fit the non-unique thermal profile was assigned to the sensor location for that given week. Thus, the calculated seepage flux is a conservative estimate for the seepage velocity when a non-unique temperature profile is observed.

Spring and Summer Seepage Flux

The solution to equation (1) assuming sinusoidal variation in surface temperature and constant temperature at depth in the streambed can be expressed as [*Hatch et al.,* 2006; *Keery et al.,* 2007; *Stallman,* 1965]:

$$T(z,t) = T_0 + A\exp(-az)\cos(\omega t - bz) \tag{6}$$

where T_0 is the average surface temperature (°C), A is the amplitude of the temperature fluctuations at the surface (°C) and ω is the angular frequency, defined as $\omega = 2\pi/P$ where P is the period of the temperature fluctuation (86,400 seconds for daily frequency). This solution can be applied with non-vertical (curvilinear) paths as long as fluxes in the directions orthogonal to the vertical do not result in a large divergence of energy fluxes within the space between the two sensors [*Cuthbert and Mackay,* 2013]. In Equation (6) the a and b terms can be expressed as:

$$a \approx \frac{-\ln\left(\frac{A_2}{A_1}\right)}{\left(z_2 - z_1\right)} = \frac{-\ln\left(\frac{A_2}{A_1}\right)}{\Delta z} \tag{7}$$

$$b \approx \frac{\phi_2 - \phi_1}{\left(z_2 - z_1\right)} = \frac{\phi_2 - \phi_1}{\Delta z} \tag{8}$$

where the subscripts 1 and 2 refer to the shallower and deeper temperature sensors, respectively and ϕ_2-ϕ_1 is the phase shift (rad) associated with two temperature sensors. The newly presented term, η, relates a and b in one single metric [*Luce et al.,* 2013]:

$$\eta = \frac{-\ln\left(\frac{A_2}{A_1}\right)}{\phi_2 - \phi_1} = \frac{\sqrt{\sqrt{v_*^4 + 4} + v_*^2} - \sqrt{2}v_*}{\sqrt{\sqrt{v_*^4 + 4} - v_*^2}} \tag{9}$$

where:

$$v_* = \frac{v_t}{v_d} \tag{10}$$

v_t is the thermal front velocity associated with advective transport of thermal energy and $v_d = \sqrt{2\omega\kappa_e}$ is the diffusive phase velocity associated with the diffusive transport of thermal energy in the streambed. η, the ratio of the logarithm of surface and depth amplitudes to the phase difference of surface and depth thermal time signals relates to the dimensionless v_* velocity, which contains both thermal front velocity (advective and diffusive) and phase velocity (diffusive) components representing different transport modes for the thermal signal. The dimensionless velocity, v_*, is one-half of the Peclet number and provides direct information on the relative importance of advective and diffusive transport. Diffusion dominates where v_*<<1 and advection dominates when v_*>>1. The analytical explicit solution relating v_* and η is [*Luce et al.*, 2013]:

$$v_* = \frac{1}{\sqrt{2}} \frac{\frac{1}{\eta} - \eta}{\sqrt{\frac{1}{\eta} + \eta}} \tag{11}$$

For η in the range of $0 < \eta < 1$ Darcian velocities are positive (i.e. downwelling). When $\eta = 1$ Darcian velocity is zero (i.e. only diffusive transport) and when $\eta > 1$ Darcian velocities are negative (i.e. upwelling).

Equation (11) combines the amplitude ratio and time lag into one metric and allows the determination of a dimensionless velocity independent of information about the depths of the sensors. The additional degree of freedom obtained from using the sensor spacing and amplitude ratio (or phase difference) can be applied to estimate the thermal diffusivity of the streambed [*Luce et al.*, 2013].

$$\kappa_e = \frac{\omega \Delta z^2}{\Delta\phi^2 \left(\frac{1}{\eta} + \eta\right)} \tag{12a}$$

$$\kappa_e = \frac{\omega \eta^2 \Delta z^2}{\ln^2\left(\frac{A_2}{A_1}\right)\left(\frac{1}{\eta} + \eta\right)} \tag{12b}$$

Both equations provide a consistent estimate for the thermal diffusivity and therefore only one should be applied. Thermal diffusivity is related to the damping depth (depth at which the amplitude is 1/e times the surface amplitude) by $z_d = \sqrt{2\kappa_e / \omega}$.

Calculation of spring and summer seepage flux as well as determination of thermal diffusivity requires the amplitude and phase angle associated with the diurnal forcing to be determined for each thermal time series. While short time series can be examined with graphical or visual methods, longer time series typically require the use of fitting functions such as nonlinear least squares fitting [*Swanson and Cardenas,* 2010] or Fourier analysis to isolate the amplitude and phase angle [*Luce and Tarboton,* 2010]. Dynamic harmonic regression (DHR), which is implemented within the MATLAB based CAPTAIN toolbox [*Taylor et al.,* 2007] was used to isolate the amplitude and phase information from thermal time series at Bear Valley Creek. DHR is a non-stationary extension to Fourier analysis and produces time varying apparent amplitude and phase coefficients for a time series at a user specified frequency (one day for this study). DHR has been used successfully in several studies to determine thermal time series characteristics and subsequently quantify streambed seepage flux [e.g. *Briggs et al.,* 2012; *Keery et al.,* 2007; *Vogt et al.,* 2010]. DHR was implemented using the new VFLUX program [*Gordon et al.,* 2012] as a front-end tool for applying a filter to the thermal time series, isolating the diurnal component (using DHR), and extracting the time varying amplitude and phase information.

The original thermal time series (Δt = 12 minutes) from 01 April 2007 through 10 July 2007 (the portion of the thermal time series that presented diurnally fluctuating surface and depth temperatures) was downsampled using a low-pass filter such that the time interval was 2 h. Using the low-pass filter eliminates much of the high frequency noise that complicates fitting of the observed thermal time series. DHR was then implemented via the CAPTAIN toolbox within VFLUX to extract the time varying apparent amplitude and phase of the temperature signal. The frequency was specified as one day (diurnal fluctuations). Following practices implemented by other DHR users, two days of the diurnal signal were removed from each end of the temperature record to eliminate possible edge effects due to filtering [*Gordon et al.,* 2012; *Keery et al.,* 2007].

The time-varying amplitude and phase information was used to calculate a time-varying η parameter (equation 9). Following the determination of η, ν_* was determined based on equation (11). Using equation (12a), thermal diffusivity was estimated for two five day periods within the period of record where the thermal time series was visually determined to approximate the idealized boundary conditions. The two five day periods selected were 08 May 2007 through 12 May 2007 and 2 July 2007 through 6 July 2007 (representing spring and summer conditions, respectively). The average of all thermal diffusivity values that demonstrated agreement between spring and summer estimates of thermal diffusivity was used to determine the value for bulk thermal diffusivity, which was used when calculating the streambed seepage flux for the entire spring/summer time period. The average thermal diffusivity value was checked to see if it fell within an appropriate range of 0.02 – 0.13 m^2 day^{-1} as reported by *Shanafield et al.* [2011].

Since DHR provides a time series of apparent amplitude and phase angle, it is possible to calculate a time-varying thermal diffusivity value at each sensor location for the entire time series. Barring drastic changes to the streambed sediments over a relatively short time scale, thermal diffusivity values should remain relatively constant through time, and the Bear Valley Creek system is expected to be characterized by relatively constant thermal diffusivity values over time. Other researchers have applied spatially varying values of thermal diffusivity for highly heterogeneous sediment [*Fanelli and Lautz,* 2008] but that distinction without *a priori* knowledge of sediment heterogeneity was not warranted for this study. We used an average bulk diffusivity value calculated from two seasonally variant time periods to estimate an average thermal conductivity. The calculated value for thermal conductivity was used during the winter seepage flux calculations and so determining a value of thermal conductivity based on the calculated bulk diffusivity value provides continuity between the two methods and maintains consistent properties of the HZ for this study.

Following the determination of the thermal diffusivity, the diffusive phase velocity was calculated for the Bear Valley Creek system. Equation (10) was then used to calculate the thermal front velocity. Thermal front velocity is related to the Darcian seepage flux by the γ term (ratio of the sediment-water matrix specific heat and water specific heat). Streambed seepage fluxes were calculated between the surface sensor and depth sensors (0 to 10 cm, 0 to 20 cm and 0 to 50 cm) from 03 April 2007 through 08 July 2007. Thus, for each location the calculations represent depth averaged seepage flux between the surface and depth sensor at 10 cm, 20 cm and 50 cm. For each of the depth averaged sensor pairings the downsampled frequency of 12 samples per day leads to 1,164 estimates of time varying seepage flux. It is important to note that the solutions for the winter, spring, and summer seepage fluxes represent only the vertical component of the seepage flux (both solutions solve the governing one-dimensional advection-diffusion equation). This one-dimensional simplification is commonly applied to HZ systems [e.g. *Fanelli and Lautz,* 2008; *Hatch et al.,* 2010; *Keery et al.,* 2007; *Lautz,* 2012]. The one-dimensional results are used to interpret aspects of three-dimensional system behavior.

Three specific five day time windows were examined to determine the spatial and temporal characteristics of HZ fluxes. Two time windows correspond to spring runoff peak flows and the third window corresponds to low flow conditions on the receding limb of the hydrograph. The first time window (01 May 2007 through 05 May 2007 – "Spring – Bankfull") is slightly below bankfull flow in Bear Valley Creek as determined from the reconstructed hydrograph. The second time window (17 May 2007 through 21 May 2007 – "Spring – Overbank") corresponds to an overbank flow event, which is seasonally quite common for the Bear Valley Creek system due to the wide alluvial valley, low elevation floodplain, and local features (wood, partial channel spanning beaver dams, etc) causing increased water surface elevations. The last time window (02 July 2007 through 06 July 2007 – "Summer – Low Flow") corresponds to low flow conditions on the receding limb of the hydrograph. Absolute low flow conditions (typically late August or September) are not represented in the available thermal time series.

Seepage Flux Direction and Velocity Errors

The error associated with η can be calculated with the following equation [*Luce et al.,* 2013]:

$$\sigma_\eta = \sqrt{\frac{\sigma_A^2}{(\phi_2-\phi_1)^2}\left(\frac{1}{A_2^2}+\frac{1}{A_1^2}\right)+2\frac{\sigma_\phi^2 \ln\left(\frac{A_2}{A_1}\right)^2}{(\phi_2-\phi_1)^4}} \tag{13}$$

where σ_A is the error associated with the amplitude measurement, σ_φ is the error associated with the time measurement, and σ_η is the absolute error on the η estimate. The error associated with v_* can be calculated with the following equation:

$$\sigma_{v_*} = \frac{1}{\sqrt{2}}\sqrt{\left[\frac{-\sqrt{\eta+1/\eta}\left(\eta^4+6\eta^2+1\right)}{2\eta\left(\eta^2+1\right)^2(\phi_2-\phi_1)}\cdot\left(\frac{1}{A_2}-\frac{1}{A_1}\sigma_A\right)\right]^2+\left[\frac{-\sqrt{\eta+1/\eta}\left(\eta^4+6\eta^2+1\right)}{\left(\eta^2+1\right)^2(\phi_2-\phi_1)}\cdot\sigma_\phi\right]^2} \tag{14}$$

where σ_{v*} is the absolute error on the v_* estimate. For this study, amplitude errors were assumed to be approximately 0.05°C and phase errors were assumed to be 0.03 rad (6.87 minutes, or approximately $\Delta t/2$).

Results

Thermal Diffusivity

Thermal diffusivity values were calculated for all monitoring locations based on the five day average amplitude, phase angle and v_* values. Only the top three sensors (0 cm, 10 cm and 20 cm) were used for the calculation since these sensors typically demonstrate the greatest diurnally fluctuating behavior. When using three sensors at each location the three combinations for sensor pairings (0 to 10 cm, 10 to 20 cm, 0 to 20 cm) produce three estimates of thermal diffusivity. Figure 5 shows the thermal diffusivity values calculated for the representative spring period (08 May 2007 – 12 May 2007) and summer period (02 Jul 2007 – 06 Jul 2007). The minimum calculated thermal diffusivity is 0.024 m^2 day^{-1} and occurs at the Downstream Pool location during the spring season. The maximum calculated thermal diffusivity is 1.03 m^2 day^{-1} and occurs at the Left Riffle location during the summer season.

It is observed that the Left Upstream Pool, Upstream Riffle, and Left Riffle locations show poor agreement between the spring and summer thermal diffusivity estimates. Similarly, the Downstream Pool location shows poor agreement between spring and summer at the 0 to 10 cm depth interval. Disregarding these locations, the maximum calculated thermal diffusivity is 0.14 m^2 day^{-1} and occurs at the Central Riffle location during the spring season. This value, along with the minimum calculated thermal diffusivity of 0.024 m^2 day^{-1}, nearly fall within the expected range as reported by *Shanafield et al.* [2011]. Possible explanations for the poor agreement at the Left Upstream Pool, Upstream Riffle, and Left Riffle locations are explored later. The reader is referred to the discussion by *Luce et al.* [2013] regarding the inconsistencies in thermal diffusivity estimates at the Downstream Pool location due to streambed scour.

The average bulk thermal diffusivity among sensors displaying consistent agreement between the two time periods is calculated to be 0.0816 m^2 day^{-1}. The thermal conductivity is calculated to be 2.56 W m^{-1} $°C^{-1}$.

Winter Seepage Flux

From 10 December 2006 through 10 March 2007, 13 weeks of steady state temperature data were analyzed at each monitoring location (117 total thermal profiles). For five weeks (4% of all profiles) at the Left Upstream Pool location, temperatures at depth did not provide a suitable thermal gradient (i.e. temperatures at 10 cm and 20 cm were outside of the boundary conditions established by the 0-cm and 50-cm sensors) and therefore no seepage flux was calculated. Twenty-three weeks (20% of all profiles) presented thermal gradients leading to a non-unique solution of the streambed seepage flux. This occurred when temperatures at 10 cm and 20 cm matched the surface or deep boundary condition such that a unique seepage flux could not be determined. The seepage flux was set at the minimum upwelling or downwelling velocity to match the observed thermal profile. This assumption may under-estimate the fluxes but it provides a systematic method for predicting the flux. Seventeen (14% of all profiles) of the calculated velocities were less than the acceptable limit as presented in equation (5), which implies that streambed heat transport is predominantly diffusive in nature, and so streambed seepage flux was estimated as zero. Seventy-two of the thermal profiles (62% of all profiles) presented streambed seepage flux solutions that were unique and within the acceptable limits as determined using equation (5). Table 1 summarizes the streambed seepage velocities calculated at each monitoring location. Figure 6 shows thermal profiles at several monitoring locations and displays the model fit for representative upwelling and downwelling conditions.

Variability in the computed weekly streambed seepage flux at the monitoring locations is shown in Figure 7. With the exception of the Right Upstream Pool and Right Riffle locations downwelling seepage fluxes are observed to persist throughout the winter season, indicating that Bear Valley Creek is predominantly losing water in the vicinity of the study site during winter. Winter is a low flow season for this high elevation site. The Left Upstream Pool location exhibits the strongest downwelling signal with a median seepage flux of 64 cm day^{-1}. The location experiencing the strongest upwelling signal is observed to be the Right Riffle monitoring location, with a median seepage flux of -25.6 cm day^{-1}. Considering the sensors in the center of the channel along the PRP sequence it is observed that the typically generalized behavior of downwelling at the head of the riffle and upwelling at the tail of the riffle into the downstream pool is not observed for Bear Valley Creek during this season. Rather, downwelling seepage fluxes are predicted for all monitoring locations along the longitudinal PRP sequence. Downwelling velocities are stronger at the upstream end and the strength of the downwelling signal decreases towards the downstream end of the PRP morphological feature. The Central Upstream Pool and Downstream Riffle monitoring locations experience a wider variability in calculated seepage fluxes than the Upstream Riffle, Central Riffle, and Downstream Pool sensor locations.

The monitoring locations positioned in the cross-channel direction exhibit a general pattern of upwelling seepage fluxes at the upvalley (river right) bank and increasingly downwelling seepage fluxes at the downvalley (river left) bank. The right bank (RUP and RR) monitoring locations both predict upwelling conditions that persist throughout the winter season. The Central Upstream Pool and Central Riffle monitoring locations predict downwelling conditions, but the median velocities predicted (59 and 19.4 cm day^{-1}, respectively) are less than the left bank monitoring locations (LUP and LR). The median downwelling fluxes for the left bank (LUP and LR) monitoring locations are 64 and 58 cm day^{-1}, respectively. Across the upstream pool (RUP-CUP-LUP) monitoring locations, the overall change in median seepage flux velocity is 72.7 cm day^{-1}, or an average cross-channel velocity gradient of approximately 4.8 cm day^{-1} m^{-1} for an average stream width of 15 m at this location. Along the riffle crest (RR-CR-LR) monitoring locations the overall change in median seepage flux velocity is 83.6 cm day^{-1}, or an average cross-channel velocity gradient of approximately 5.6 cm day^{-1} m^{-1} for an average stream width of 15 m.

Spring and Summer Seepage Flux

The VFLUX and DHR tools provide a time varying apparent amplitude and phase angle associated with the diurnal frequency of the original thermal time series, sampled at the user-specified interval of 12 observations per day. The fit obtained with DHR is shown in Figure 8 for the Downstream Pool and Left Upstream Pool locations during the “Spring – Bankfull” and “Summer – Low Flow” time windows. Similar fits were obtained for the temperature observations at the other monitoring locations. The variability of calculated seepage fluxes is demonstrated with box-and-whiskers plots (Figure 9) representing the entire period analyzed (03 Apr 2007 – 08 Jul 2007), the “Spring – Bankfull” (01 May 2007 through 05 May 2007), “Spring – Overbank” (17 May 2007 through 21 May 2007) and “Summer – Low Flow” (02 July 2007 through 06 July 2007) time windows.

Viewing the spatial arrangement of seepage fluxes in the stream, rather than with box-and-whiskers plots, can offer additional insight into the spatial and temporal characteristics of the HZ flux results. Figure 10 shows the median seepage fluxes, represented as point fluxes, for the entire period, the “Spring – Bankfull”, “Spring – Overbank”, and “Summer – Low Flow” time windows for the 0 to 20 cm depth averaged interval. Over the entire period, longitudinal fluxes are observed to be downwelling at the Upstream Riffle location and transitional at the Central Upstream Pool and Central Riffle locations. The Downstream Riffle and Downstream Pool locations predict upwelling fluxes. The right bank (RUP and RR) locations predict upwelling seepage fluxes. The Left Riffle location predicts downwelling seepage fluxes and the Left Upstream Pool location is transitional. The general gradient along the upstream pool monitoring location (RUP-CUP-LUP, following the valley gradient) sensor profile is from upwelling to increasingly transitional seepage flux. The gradient along the riffle crest (RR-CR-LR) sensor profile is from upwelling to increasingly downwelling seepage flux. At the upstream pool (RUP-CUP-LUP) monitoring locations the overall change in median seepage flux velocity is 1.5 cm day^{-1}, or an average cross-channel velocity gradient of approximately 0.1 cm day^{-1} m^{-1} for an average stream width of 15 m at this location. Along the riffle crest (RR-CR-LR) monitoring locations the overall change in median seepage flux velocity is 29.2 cm day^{-1}, or an average cross-channel velocity gradient of approximately 1.9 cm day^{-1} m^{-1} for an average stream width of 15 m.

During the “Spring – Bankfull” period the sensors display predominantly upwelling seepage fluxes along the longitudinal profile. The Central Upstream Pool and Central Riffle sensors predict transitional seepage fluxes, and it is observed that the strength of upwelling seepage flux increases in the downstream direction. All cross-channel sensors predict upwelling seepage fluxes. Along the upstream pool (RUP-CUP-LUP) sensor profile upwelling fluxes are observed to be strongest near the channel banks and weakest near the center of the channel. A similar pattern is observed along the riffle crest (RR-CR-LR) sensor profile.

During the “Spring – Overbank” period along the longitudinal profile the Central Upstream Pool and Upstream Riffle sensors predict downwelling seepage flux velocities. The Central Riffle sensor is transitional and strong upwelling fluxes are observed at the Downstream Riffle and Downstream Pool locations. The cross-channel sensors predict mixed behavior at this depth, with the Right Riffle and Left Upstream Pool sensors predicting upwelling seepage fluxes while the Right Upstream Pool and Left Riffle sensors predict downwelling seepage fluxes. Along the upstream pool (RUP-CUP-LUP) sensor profile the gradient of seepage fluxes is from downwelling to upwelling conditions. Conversely, along the riffle crest (RR-CR-LR) sensor profile the gradient is from upwelling to downwelling conditions. At the upstream pool (RUP-CUP-LUP) monitoring locations the overall change in median seepage flux velocity is 18.7 cm day^{-1}, or an average cross-channel velocity gradient of approximately 1.2 cm day^{-1} m^{-1} for an average stream width of 15 m at this location. Along the riffle crest (RR-CR-LR) monitoring locations the overall change in median seepage flux velocity is 18.8 cm day^{-1}, or an average cross-channel velocity gradient of approximately 1.3 cm day^{-1} m^{-1} for an average stream width of 15 m.

During the “Summer – Low Flow” period seepage fluxes along the longitudinal profile predict transitional fluxes at the Central Upstream Pool location, downwelling at the Upstream Riffle location, and upwelling fluxes for the Central Riffle, Downstream Riffle, and Downstream Pool locations. The right bank (RUP and RR) sensors predict upwelling seepage fluxes while the left bank (LUP and LR) sensors predict downwelling seepage fluxes. Along the upstream pool (RUP-CUP-LUP) and riffle crest (RR-CR-LR) sensor profiles the seepage flux gradient transitions from upwelling-diffusive-downwelling flux conditions. At the upstream pool (RUP-CUP-LUP) monitoring locations the overall change in median seepage flux velocity is 13.7 cm day^{-1}, or an average cross-channel velocity gradient of approximately 0.9 cm day^{-1} m^{-1} for an average stream width of 15 m at this location. Along the riffle crest (RR-CR-LR) monitoring locations the overall change in median seepage flux velocity is 61.8 cm day^{-1}, or an average cross-channel velocity gradient of approximately 4.1 cm day^{-1} m^{-1} for an average stream width of 15 m. The magnitude of the seepage flux is observed to be greater at the cross-channel sensors than that near the center of the channel.

Seepage Flux Direction and Velocity Errors

Equation (13) was used to estimate the absolute (+/- 1σ) error on calculations of η. Equation (14) was used to estimate the absolute (+/- 1σ) error on calculations of v_*. The coefficient of variation was calculated for v_* ($CV = \sigma_{v_*} / |v_*|$) and represents the percentage error associated with the v_* calculations.

Figure 11, panels A1, B1 and C1, shows the coefficient of variation, v_* and error bounds on the estimate of the η parameter at a depth of 10 cm for the entire time period at the Downstream Riffle monitoring location. Estimates of η confirm that the Downstream Riffle location experiences almost exclusively upwelling seepage fluxes at the 10 cm depth. Where the confidence intervals defined by the $\eta \pm \sigma_\eta$ lines are inclusive of a value of 1 (the transition line between upwelling and downwelling flows) the true direction of the hyporheic flux is uncertain at the confidence level of one standard deviation. This uncertainty occurs for 4.6% of the estimates at the Downstream Riffle sensor location. Estimates of v_* reflect the pattern of predominantly upwelling seepage fluxes. When the v_* estimate is very near to zero, the coefficient of variation related to v_* predicts very high percentage errors. These errors are due to the near zero v_* estimates so the actual magnitude of errors applied to v_* would be small. The median coefficient of variation is +/- 0.6 and 98.7% of the estimates are calculated to be within an order of magnitude of the true v_* magnitude.

Figure 11, panels A2, B2 and C2, shows the coefficient of variation, v_* and error bounds on the estimate of the η parameter at a depth of 20 cm for the entire time period at the Left Riffle monitoring location. Error bounds on the η parameter indicate increased uncertainty on the calculated direction during the first half of the time series. Confidence intervals on the direction of flow defined by the $\eta \pm \sigma_\eta$ lines indicate that 52% of the estimates have an uncertain flow direction at the confidence level of one standard deviation. The coefficient of variation for v_* indicates high percentage errors when the v_* estimate is very near to and crossing the upwelling/downwelling transition line. During the late spring and early summer period, predominantly downwelling conditions establish at the 20 cm depth and errors in the estimate of v_* show a marked reduction. The median coefficient of variation is +/- 1.1 and 96.1% of estimates are within an order of magnitude of the true v_* magnitude.

Figure 11, panels A3, B3 and C3, shows the coefficient of variation, v_* and error bounds on the estimate of the η parameter at a depth of 50 cm for the entire time period at the Upstream Riffle monitoring location. Confidence intervals on the direction of flow defined by the $\eta \pm \sigma_\eta$ lines indicate very high uncertainty on the calculated direction during the entire time series. The coefficient of variation for v_* indicates high percentage errors when the v_* estimate is very near to and crossing the upwelling/downwelling transition line. Velocities during this time are low, so actual magnitude errors would likely be small. The median coefficient of variation is +/- 6.1. Approximately 69% of calculated v_* values are predicted to be within an order of magnitude of the true or v_* magnitude.

Discussion

Thermal Diffusivity

Calculated values for thermal diffusivity demonstrate consistent agreement between spring and summer time windows for the Central Upstream Pool, Right Upstream Pool, Central Riffle, Right Riffle, Downstream Riffle, and Downstream Pool (with the exception of 0 to 10 cm at DP) locations. The ability to calculate a thermal diffusivity value based on equations (12a) and (12b) demonstrates an advantage of using the presented method wherein phase angle and amplitude ratio are combined into one metric to calculate seepage flux. Using one combined metric to estimate velocity allows for the additional degree of freedom existing in the calculation to be applied to estimates of the thermal diffusivity term using either the phase angle or amplitude ratio of temperature sensors at two known depths. Current work typically requires estimates of bulk thermal diffusivity, which as many have pointed out takes on values over a considerably smaller range than, for example, hydraulic conductivity [*Fanelli and Lautz,* 2008; *Lapham,* 1989]. Still, identifying a procedure for obtaining site specific thermal diffusivity estimates presents an advance over current methodologies and allows for better characterization of the HZ environment.

Further examination of the cause of the discrepancies between the spring and summer estimates of thermal diffusivity at the Left Upstream Pool, Upstream Riffle, Left Riffle, and Downstream Pool (0 to 10-cm) sensors reveals patterns in the results that are informative. First, when spring and summer estimates of thermal diffusivity are compared the values estimated for summer diffusivity are nearly always higher than those estimated during spring. The notable exception to this is the 0 to 10 cm estimate at the Downstream Pool location. Second, the calculated thermal diffusivity value for the 0 to 10 cm depth during the summer time window is typically greater than estimates of thermal diffusivity at the 10 to 20 or 0 to 20 cm depth intervals. This result is observed at the Left Upstream Pool and Left Riffle locations but is not as strongly present at the Upstream Riffle location. Lastly, considering the spatial arrangement of the monitoring locations reveals that the sensors displaying differing values from the spring to summer time windows are grouped at the upstream and towards the river left portion of the study site. Differences between spring and summer estimates are greatest at the river left sensors (LUP and LR) than at the more central Upstream Riffle sensor location.

During the spring time window, seepage flux at the left bank (LUP and LR) sensor locations is predicted to be predominantly upwelling. The Upstream Riffle location predicts a mix of upwelling and downwelling seepage fluxes, although the magnitude of downwelling flux is relatively small (median flux of 9.8 cm day^{-1} at a depth of 10 cm). During the summer time window, seepage flux at the left bank (LUP and LR) sensors transitions to predominantly downwelling conditions which is a reversal in flow direction from the spring time window. The Upstream Riffle location predicts stronger downwelling conditions during the summer time window (median flux of 17.1 cm day^{-1} at a depth of 10 cm). Upwelling conditions (which were more prevalent during the spring time window) lead to thermal profiles at depth that are typically more damped in amplitude than occurs for downwelling conditions [*Luce et al.,* 2013].

Figure 12 shows the raw thermal time series for the Left Upstream Pool, Upstream Riffle, and Left Riffle locations during the spring and summer time windows. The profiles during the spring time window display temperature signals at depth that are more damped and experience slightly longer phase shifts than the profiles at the same location during the summer time window. At the Left Riffle location during the summer time window, visually analyzing the temporal shift between the surface sensor and the sensor at 20 cm clearly shows that the signal is penetrating to shallow depths very quickly. The five day average phase angle shift between the 0 cm and 20 cm sensor from DHR for this time period is 0.33 rad (approximately 75 minutes). The time shifts observed in the raw thermal record and with DHR are well below the smoothed (2 h) interval of the time series used for the DHR analysis, so high frequency components of the temperature signal at strongly downwelling locations could be misrepresented by the DHR amplitude and phase parameters (timing errors appear to be more probable due to temperature peaks that span several Δt measurements). Adjusting the phase shift parameter to a value slightly greater than that reported by DHR analysis leads to a reduction in the estimated thermal diffusivity, as can be seen based on the relationship between κ_e and $\Delta\phi$ in equation (12b).

Visually analyzing thermal signals at the Left Riffle location, if the DHR phase shift is increased (shifted later in time) by 0.12 rad (28 min) from 0 to 10 cm, 0.12 rad (28 min) from 10 to 20 cm and 0.14 rad (32 min) from 0 to 20 cm then the estimates for thermal diffusivity at the Left Riffle location are much nearer to the spring estimates (Figure 13). The shifts applied to the time series are within a reasonable range based on visually analyzing the raw thermal time series. Since DHR is using a smoothed (2 h interval) time series to fit time varying amplitude and phase parameters, then this fine temporal scale variability could be lost by the final DHR estimates of amplitude and phase angle. At the Left Upstream Pool location shifts later in time of 0.17 rad (40 min) from 0 to 10 cm, 0.07 rad (16 min) from 10 to 20 cm and 0.24 rad (56 min) from 0 to 20 cm lead to estimates of thermal diffusivity that approach spring estimates. Lastly, at the Upstream Riffle location shifts of 0.07 rad (16 min) from 0 to 10 cm, 0.05 rad (12 min) from 10 to 20 cm and 0.10 rad (23 min) from 0 to 20 cm lead to improved agreement between spring and summer diffusivity estimates (Figure 13). All of the phase shifts were visually checked against the raw thermal time series and the possible shift appears to be reasonable (i.e. phase angle used for adjusted summer thermal diffusivity estimate can be observed at points in the raw temperature series). Also, all adjustments are within the 2 h smoothing interval that was applied prior to the DHR analysis, so this behavior seems to be consistent with small phase differences that would tend to occur in moderate to strongly downwelling conditions.

At the Downstream Pool location during the spring time window the thermal diffusivity estimate from 0 to 10 cm is much higher than other estimates during spring and all estimates during the summer time window. The Downstream Pool location consistently experiences upwelling conditions during the spring season, so errors in thermal diffusivity are not likely to be due to small temporal differences occurring as a result of strongly downwelling seepage fluxes. *Luce et al.* [2013] associated the discrepancy to scour and depositional processes, which may occur at that location. If a significant amount of scour is possible from 0 to 10 cm during the spring season, then the value estimated for thermal diffusivity would be in error since Δz was assumed to be 10 cm (sediment-water matrix thickness).

Because the thermal properties of the sediment should be constant with time unless substantial changes in sediment porosity occur, *Luce, et al*. [2013] proposed the following equation to calculate the sediment thickness variations between sensors based on time-invariant effective thermal diffusivity of the sediment:

$$\Delta z(t) = \frac{-\log(A_r(t))}{\eta(t)}\sqrt{\frac{\kappa_e}{\omega}\left(\frac{1}{\eta(t)}+\eta(t)\right)} = \Delta\phi(t)\sqrt{\frac{\kappa_e}{\omega}\left(\frac{1}{\eta(t)}+\eta(t)\right)} \quad (15)$$

Note the explicit dependence on time for Δz, η, A_r and ϕ, whereas κ_e is constant after being evaluated earlier.

Executing this calculation results in a Δz value (for 0 to 10 cm) of 2 cm, which corresponds to an estimated scour depth of 8 cm. For a depth of 0 to 20 cm the Δz value is calculated to be 14.8 cm, which corresponds to an estimated scour depth of 6.2 cm. The indication that scour may be most likely to occur at the Downstream Pool location during peak flow events is consistent with the findings of *Caamano et al.* [2012] that pools experience high shear stresses during flood events.

Winter Seepage Flux

Winter, spring and summer seasons demonstrate considerable variability in streambed seepage fluxes in Bear Valley Creek. During the winter, the longitudinal PRP sensors consistently predict losing conditions. This behavior is shown conceptually on Figure 14 (see Figure 2 for a schematic of theoretical profile alignments the Figure 14 sections represent). The magnitude of losing fluxes appear to be modulated by the streambed topography, since the farthest downstream (DR and DP) sensors predict much smaller downwelling fluxes than the upstream (CUP, UR and CR) sensors. It is unlikely that the entire Bear Valley Creek reach is losing during the winter season. Headwater systems such as Bear Valley Creek are typically gaining, although sub-reaches within the headwaters can experience both gaining and losing conditions at various times [*Winter et al.,* 1998].

A reduction in the strength of downwelling flows for the Downstream Riffle and Downstream Pool sensors is also apparent by studying the thermal profiles (for example, see Figure 6, DP location). Temperatures at depth for the Downstream Riffle and Downstream Pool sensors are much higher than temperatures at depth for the upstream sensors, so even though slightly downwelling conditions are observed, the strength of the downwelling flux is insufficient to rapidly cool the pore water at these locations. Strongly downwelling locations were observed to quickly approach depth temperatures that mimic those of the surface water (for example, see Figure 6, UR location). In a study of seasonal hyporheic temperature dynamics, *Hannah et al.* [2009] reported warmer temperatures at depth in the tails of two riffles during the winter season, similar in behavior to what is observed for Bear Valley Creek. In their study, shallow and deep temperatures at the head of the riffles were much more similar (depths down to 40 cm) than were comparisons of shallow and deep temperatures at the riffle tail [*Hannah et al.,* 2009]. Similarly, *Krause et al.* [2011] reported warmer riffle tail temperatures at depth than riffle head temperatures even though generally upwelling conditions were predicted for the entire PRP morphological feature studied. The findings that streambed pore water temperatures at the riffle tail tend to be warmer than at the riffle head are consistent with the conceptualization that these areas should tend towards upwelling conditions based on streambed topography. Bear Valley Creek data demonstrate that even if slightly losing conditions occur, the reduced magnitude of cold downwelling fluxes may not cause hyporheic water in the riffle tail to become as cold as other areas such as the riffle head due to diffusive heat transport.

Seepage fluxes near the edges of the channel during the winter season show that upvalley (river right) areas are characterized by upwelling fluxes while downvalley (river left) areas are characterized by downwelling fluxes (Figure 14 demonstrates this conceptual behavior). The upwelling areas experience warmer pore water conditions than downwelling areas during the winter season, and these thermal conditions affect ecological and biogeochemical reactions [*Cardenas and Wilson,* 2007; *Marzadri et al.,* 2013]. The spatial arrangement of upwelling to downwelling along the transverse gradient could create thermal gradients that are important for aquatic species such as Chinook salmon, whose embryos incubate over the winter season. Warmer temperatures in upwelling areas could reduce the risk of mortality due to freezing and ensure optimal emergence times [*Geist and Dauble,* 1998]. Salmonid embryos may survive and develop normally at temperatures even below the threshold limit of 5°C as long as their development progressed long enough to enable them to tolerate cold temperature [*Bjornn and Reiser,* 1991]. However, cold temperatures near freezing will increase the incubation period and may lead to smaller hatching fish. Seepage flux magnitudes near the channel sides were generally greater than magnitudes near the center of the channel, which supports the findings of *Storey et al.* [2003]. The average of the median downwelling fluxes for the channel-edge sensors during the winter was 61 cm day^{-1}, which is approximately twice as large as the average of the median downwelling fluxes for the center channel sensors of 29.1 cm day^{-1}.

Spring and Summer Seepage Flux

Whereas winter seepage fluxes were calculated in one depth-averaged profile (0 to 50 cm), the methodology used to calculate spring and summer seepage fluxes utilizes three sensor pairings (0 to 10 cm, 0 to 20 cm and 0 to 50 cm) to calculate depth-averaged seepage fluxes in each of the three depth intervals. As a result, the flux results during the spring and summer seasons represent the depth-averaged behavior for the near surface sensors (10 and 20 cm) as well as for a deeper profile extending from the surface down to the 50-cm sensor. The seepage fluxes calculated for each sensor location are representative of the dominant flux direction over the entire depth interval.

During near bankfull flow events, the longitudinal PRP sequence exhibits downwelling and upwelling characteristics consistent with the classic PRP hyporheic flux behavior at shallow depth intervals (10 and 20 cm, Figure 14) [*Marzadri et al.,* 2010; *Tonina and Buffington,* 2007]. At a depth of 50 cm all sensors indicate upwelling seepage flux, which demonstrates that the active downwelling hyporheic zone likely does not extend past 50 cm at the study site during this time period. The overall signal between the surface and 50 cm is an upwelling signal as indicated by the results using the 0-cm and 50-cm sensors. In the center of the channel, the 50 cm depth averaged behavior is influenced by the PRP streambed topography. This is observed in the 10 cm and 20 cm interval results, where sensors at the upstream pool and riffle head locations predict depth-averaged downwelling flows. The results demonstrate that in the vicinity of the study site Bear Valley Creek is, overall, gaining during the near bankfull period, but shallower streambed sediments are still influenced by local topography features such as the PRP sequence. This is consistent with previous studies, which suggested that hyporheic exchange is primarily a near surface processes [*Marzadri et al.,* 2010], and with the conceptual model that local topography should control upwelling and downwelling areas [e.g., *Tonina and Buffington,* 2009a]. Sensors near the edge of the channel display upwelling conditions at all depths. Upwelling behavior near the channel banks is consistent with the findings of *Whiting and Pomeranets* [1997] that bank discharge to the stream occurs during periods of high bank water table gradients (i.e., when bank water table is above the water surface elevation). This behavior is very likely in Bear Valley Creek during this time, since early season snowmelt would likely be recharging the local ground water aquifer and leading to saturated bank conditions while runoff from higher in the watershed is not as strong as it is later.

During overbank flow events, patterns of hyporheic exchange are more complex. Along the longitudinal gradient the pattern of downwelling and upwelling according to the classic PRP model is observed at depths of 10 and 20 cm (Figure 14). Again, at 50 cm depths the general signal is predominantly upwelling. The depth-averaged signal that is predominantly upwelling for the 0 cm to 50 cm interval again indicates that the system tends to be gaining during high discharge periods, which is to be expected in a headwater stream. The differing directions predicted in the center of the channel for the shallower depth intervals (0 to 10 cm and 0 to 20 cm) indicates that the local streambed topography continues to induce shallow downwelling-to-upwelling cells during these events.

The sensors near the edges of the channel demonstrate varied behavior. The Left Upstream Pool and Right Riffle sensors predict upwelling behavior at 10 and 20 cm, while the Left Riffle sensor predicts upwelling at both 10 and 20 cm and the Right Upstream Pool sensor predicts upwelling at a depth of 20 cm. Fluxes at 50 cm are transitional for the Left Upstream Pool, Right Upstream Pool, and Left Riffle sensors although the Right Riffle sensor still displays a strong upwelling signal. The patterns of upwelling and downwelling signals at the channel edges during this time window are not clearly grouped by upvalley or downvalley locations. One possible explanation for this behavior could be that superelevation of the water surface at the upstream pool location created a head differential that resulted in downwelling flows at the right side of the channel and upwelling flows at the left side of the channel. Numerical modeling results for bankfull conditions do indicate that a superelevated water surface exists at the upstream pool location and that water surface elevation is higher near the right bank than at the left bank [data from *Tonina and McKean,* 2010 and; *Tonina et al.,* 2011]. During overbank flow events the superelevation feature could be locally enhanced by the formation of eddies or complex flowpaths in the floodplain area [*Shiono et al.,* 1999].

Alternatively, the behavior could be the result of differing water sources (recent melt and long bank storage) according to work presented by *McGlynn et al.* [2005] and therefore the thermal signal could be influenced by a mixing of surface water and longer residence time bank water. *Claxton et al.* [2003] found that overbank flows can "hold back" hillslope and possibly bank-retained water due to the steep hydraulic gradient induced by flood waters; so seemingly disconnected hyporheic fluxes could result from this complex behavior. Lastly, *Wroblicky et al.* [1998] reported variation in lateral hyporheic area during flooding events, so local expansion or contraction of lateral hyporheic zones could cause varied behavior as well.

Summer low flow conditions demonstrate PRP fluxes consistent with the classical conceptualization model at depth-averaged intervals of 10 and 20 cm (Figure 14). Fluxes for the depth averaged 0 cm to 50 cm interval again show a trend towards upwelling conditions, indicating that the hyporheic zone may not extend much past 50 cm during this time window. The predominant upwelling signal predicted using the 0 to 50 cm depth interval indicates that during the receding limb of the hydrograph the overall subsurface flows are towards the stream and gaining conditions persist at the study site. For sensors in the center of the channel, the predominant upwelling signal is modulated by the streambed topography, and shallower streambed sediments experience predominantly downwelling conditions at the upstream pool and riffle head. Towards the downstream end near the riffle tail, the upwelling tendency predicted for the depth averaged 0 to 50 cm interval is complemented by the streambed topography induced upwelling, and shallow upwelling fluxes are strong near the riffle tail. Sensors near the edges of the channel predict upwelling flows on the upvalley side and downwelling flows on the downvalley side of the channel. At depths of 20 and 50 cm, a considerable gradient is observed in the transverse direction where strongly upwelling flows transition to strong downwelling conditions moving from the upvalley to downvalley portion of the stream. Flux magnitudes near the edges of the channel are again generally consistent with the findings of *Storey et al.* [2003] that lateral fluxes are stronger than mid-channel fluxes.

Seepage Flux Direction and Velocity Errors

The propagation of errors in the η term demonstrates the uncertainty in determining the direction of the seepage flux due to errors in measuring the thermal signal. In addition, field conditions are known to typically violate the boundary conditions of the 1D analytical solution [*Ferguson and Bense,* 2011]. Heterogeneities in streambed substrates could also lead to errors in calculating seepage fluxes [*Ferguson and Bense,* 2011; *Schornberg et al.,* 2010]. Results from errors relating to the η term indicate that uncertainties on the overall direction of flow will be more prominent when conditions are predominantly diffusive (e.g. near zero fluid velocity). For the Bear Valley Creek results, diffusive conditions were most commonly observed at a depth of 50 cm at the upstream sensor locations (sensors that would classically be thought of as being in a downwelling location). Similarly, uncertainties in the direction of the seepage flux occur locally when seepage fluxes are transitioning between upwelling and downwelling conditions. For the Bear Valley Creek results, transitional behavior was commonly observed at the sensors near the edges of the channel during the spring season. After the recession of flood waters, sensors near the edges of the channel such as the Left Riffle sensor established more consistent flux behavior and subsequent errors on the directional estimates were unlikely. Locations that experienced very little directional change and advective seepage flux rarely indicated possible errors in estimating the direction of exchange. Locations such as the Right Riffle, Downstream Riffle, and Downstream Pool sensors in Bear Valley Creek (predominantly upwelling across all seasons) predicted very little error on the directional estimate.

Errors on the v_* term, and subsequently the potential for errors in the predicted flux velocity, were typically within two folds of magnitude of the true velocity. Based on findings by *Ferguson and Bense* [2011], flux estimates on the order of 10 cm day^{-1} in Bear Valley Creek would likely provide good estimates of the true flux magnitude as long as variance in $\ln(K)$ is less than 1.0 $m^2 s^{-1}$. Typically order of magnitude estimates for seepage fluxes are considered to be informative, even if the true seepage flux value cannot be precisely measured from temperature data alone. One advantage of using the combined amplitude and phase metric in the η term is that separate error analyses are not required for the propagation of errors relating to the amplitude or phase angle measurements [*Lautz,* 2010; *Shanafield et al.,* 2011]. The overall effect of errors due to measuring phase and amplitude can be tracked in one error propagation exercise. Additionally, uncertainty on the flux direction depends only on measured quantities and it does not depend on the a-priori information of the effective thermal properties of the sediment or distance between sensors.

Ecological Context

An understanding of spatio-temporal hyporheic fluxes is an important link for determining habitat characteristics within the hyporheic zone across seasons and related to spatial position in the stream. Bear Valley Creek supports Chinook salmon spawning and rearing activities, and hyporheic zone processes are vital for Chinook salmon during the egg incubation portion of their lifecycle. Chinook salmon deposit their eggs into redds constructed in the hyporheic zone sediments. Eggs are typically buried from 15 to 50 cm [*DeVries,* 1997] and incubation occurs from September to early spring [*Isaak et al.,* 2007]. Incubation rates and survival of embryos and alevins are not only temperature related [*Alderdice and Velsen,* 1978; *Beacham and Murray,* 1990], but also linked to the streambed seepage flux velocity since low water velocities can possibly lead to anoxic conditions and high mortality [*Geist and Dauble,* 1998; *Tonina and Buffington,* 2009b].

Researchers have reported differing results on the spawning preferences of Chinook salmon based on upwelling or downwelling areas. *Geist and Dauble* [1998] reported that upwelling areas are preferable for Chinook salmon spawning while *Geist et al.* [2002] reported that downwelling areas were observed at Chinook spawning locations. *Isaak et al.* [2007] reported that Bear Valley Creek spawning activity is typically observed near the riffle crest, which may be a transitional area regarding upwelling or downwelling flow although lateral hyporheic velocities could provide significant horizontal fluxes through the redd. It has been posited that perhaps the presence of hyporheic exchange is more relevant than the direction of such exchange [*Geist and Dauble,* 1998].

The results obtained in this study indicate that predominantly upwelling locations (RR, DR, DP) could provide warmer winter temperatures and more stable flux conditions. Mid-channel PRP sensor locations tend to experience more stable fluxes, although temperatures towards the upstream end of the PRP sequence were observed to be much colder than downstream sensor locations. Other sensors near the edges of the channel (RUP, LUP, LR) experience a wide range of hyporheic fluxes throughout the winter and early spring, and therefore could alternate between acceptable and unacceptable habitat conditions for Chinook salmon embryos. Fluxes at 50 cm that are predominantly diffusive indicate that deeper redds may not be provided with sufficient flows to provide acceptable oxygen levels or sufficient removal of waste products [*Tonina and Buffington*, 2009b]. Further work to study the relationship of fluxes and temperature to Chinook salmon or other salmonids spawning and rearing habitat would be beneficial.

Conclusions

Two different methods were used to quantify 1-D streambed seepage fluxes using thermal time series. By using two different methods streambed seepage fluxes were calculated over a long time period (winter, spring and summer). For spring and summer flux calculations, using a single metric that combines thermal signal amplitude and phase information rather than separating this information as in previous studies demonstrated the potential use of thermal time series to obtain additional information such as thermal diffusivity or streambed scour. For strongly downwelling seepage fluxes, estimates of thermal diffusivity were observed to be greater than expected values. Adjustments to the phase angle using visual observations of the raw thermal signal provided estimates of thermal diffusivity more consistent with other time periods and locations. Applying this method for future studies could require well-behaved thermal time series collected during periods of reduced hydrologic variability to produce reliable estimates of thermal diffusivity. Using tools such as DHR could also provide time varying estimates of thermal diffusivity, and could be informative for selecting periods where the calculated thermal diffusivity is expected to best represent the system. These potential applications require additional study and validation but show great promise based on results obtained in this study.

Patterns of seepage flux were observed to be influenced by the PRP sequence (longitudinally) as well as the overall valley gradient (cross-channel) during all seasons. Cross-channel gradients can produce seepage fluxes that differ markedly from the longitudinal PRP conceptualization, as is particularly evident in this study during the summer season along the riffle crest at the Right Riffle, Central Riffle and Left Riffle locations. Cross-channel gradients led to upwelling fluxes on the upvalley side of the stream channel and strongly downwelling fluxes on the downvalley side of the stream channel. Flux magnitudes at near-bank locations tended to be of a comparable or larger magnitude when compared to seepage fluxes predicted near the center of the channel.

The analysis of errors indicates that directional errors resulting from uncertainties in the measurement of the system are proportionally the largest at low velocities, which were commonly observed for the 0-50 cm interval. This behavior likely indicates that hyporheic exchanges are damped near a depth of 50 cm and the subsequent composition of water may include some mixing from shallow ground water. Directional errors were also observed to occur when fluxes were transitional, and switched between upwelling and downwelling conditions. Directional errors were observed to be unlikely for areas that experienced strongly advective fluxes and almost no transitional behavior between upwelling and downwelling conditions. Errors on the magnitude of flux velocity estimates were estimated to be mostly within two folds of magnitude of the true flux velocity.

Understanding the complex nature of seepage fluxes and associated thermal regime of streambed sediments through time directly influences aquatic habitats and provides an understanding of the variability that is present within the hyporheic zone of streams. The use of the hyporheic zone in Bear Valley Creek by Chinook salmon for spawning activities indicates that stable, upwelling conditions will occur on the downstream side of the PRP sequence and towards the upvalley portion of the channel. These areas will also be characterized by warmer hyporheic temperatures. Stable downwelling conditions are typically observed at the upstream end of the PRP sequence near the center of the channel, although temperatures are much colder during the winter season. The riffle crest was observed to be transitional between upwelling and downwelling flows, although a horizontal flux may be present that results in increased magnitudes of flux velocities. Sensors near the edges of the channel experience large seasonal shifts in upwelling and downwelling characteristics and may be too variable for consistent habitat conditions to establish. Lastly, deeper spawning activities may result in long travel time conditions, which could slow the supply of oxygen or removal of waste products from redds.

To our knowledge no other study has combined several techniques to extend the analysis throughout multiple seasons. For high elevation systems such as Bear Valley Creek, this multiple analysis method can provide valuable insight into the hyporheic zone characteristics over several seasons.

Acknowledgements

We thank Carolyn Bohn for assistance installing the wells, and Jim McKean for providing materials and time for the initial measurements and background information for the interesting Bear Valley Creek experimental reach. This manuscript was greatly improved by the thorough examination and thoughtful comments from three anonymous reviewers. Partial funding was provided for Frank Gariglio by the US Forest Service Department of Agriculture, RJVA 10-JV-11221634-247.

Symbols and Notations

A	amplitude of thermal oscillations, °C
c	specific heat of sediment-water matrix, J kg^{-1} °C^{-1}
c_f	specific heat of water, J kg^{-1} °C^{-1}
L	length of measured sediment zone, m
n	sediment porosity, (-)
P	period of temperature oscillations, s
q	Darcy flux, m s^{-1}
t	time, s

T	temperature, °C
T_0	average surface water temperature, °C
u	pore water velocity, m s^{-1}
v_d	diffusive phase velocity, m s^{-1}
v_t	thermal front velocity, m s^{-1}
v_*	v_t/v_d, ratio of thermal front velocity to diffusive phase velocity, (-)
z	depth, positive down, m
z_d	damping depth, depth at which amplitude is 1/e times the surface amplitude, m
γ	$\rho c/\rho_f c_f$, ratio of heat capacity of sediment-water matrix to heat capacity of water, (-)
η	$-\ln\left(\frac{A_2}{A_1}\right)\Big/\phi_2-\phi_1$, ratio of negative logarithm of amplitude ratio (deep sensor divided by shallow sensor) to phase difference (deep sensor minus shallow sensor), (-)
κ_e	effective thermal diffusivity, m^2 s^{-1}
λ_0	thermal conductivity of sediment-water matrix, W m^{-1} °C^{-1}
ρ	density of sediment-water matrix, kg m^{-3}
ρ_f	density of water, kg m^{-3}
σ_A	absolute error associated with estimating the amplitude of the thermal oscillations, °C
σ_{v*}	absolute error associated with estimating v*, (-)

σ_η absolute error associated with estimating η, (-)

σ_ϕ absolute error associated with estimating phase angle of the thermal oscillations, rad

ϕ phase angle of thermal oscillations, rad

ψ $c_f \rho_f q L / \lambda_0$, (-)

ω angular frequency of thermal oscillations, rad

References

Alderdice, D. F., and F. P. J. Velsen (1978), Relation between temperature and incubation time for eggs of Chinook Salmon (*Oncorhynchus tshawytscha*), *Journal of the Fisheries Research Board of Canada*, *35*, 69-75.

Arriaga, M. A., and D. I. Leap (2006), Using solver to determine vertical groundwater velocities by temperature variations, Purdue University, Indiana, USA, *Hydrogeology Journal*, *14*, 253-263.

Baxter, C. V., F. R. Hauer, and W. W. Woessner (2003), Measuring groundwater–stream water exchange: new techniques for installing minipiezometers and estimating hydraulic conductivity, *Transactions of the American Fisheries Society*, *132*, 493–502.

Beacham, T. D., and C. B. Murray (1990), Temperature, egg size, and development of embryos and alevins of five species of Pacific salmon: a comparative analysis, *Transactions of the American Fisheries Society*, *119*, 927-945.

Bencala, K. E., M. N. Gooseff, and B. A. Kimball (2011), Rethinking hyporheic flow and transient storage to advance understanding of stream-catchment connections, *Water Resources Research*, *47*, W00H03.

Bjornn, T. C., and D. W. Reiser (1991), Habitat requirements of salmonids in streams, in *Influence of forest and rangeland management on salmonid fishes and their habitats*, edited by W. R. Meehan, pp. 83-138, Am. Fish. Soc. Spec. Publ. 19. Bethesda, Md.

Boano, F., C. Camporeale, and R. Revelli (2010), A linear model for the coupled surface-subsurface flow in a meandering stream, *Water Resources Research*, *46*, W07535.

Bredehoeft, J. D., and I. S. Papadopulos (1965), Rates of vertical groundwater movement estimated from the earth's thermal profile, *Water Resources Research*, *1*, 325-328.

Briggs, M. A., L. Lautz, J. M. McKenzie, R. P. Gordon, and D. Hare (2012), Using high-resolution distributed temperature sensing to quantify spatial and temporal variability in vertical hyporheic flux, *Water Resources Research*, *48*, W02527.

Bruno, M. C., B. Maiolini, M. Carolli, and L. Silveri (2009), Impact of hydropeaking on hyporheic invertebrates in an Alpine stream (Trentino, Italy), *International Journal of Limnology*, *45*, 157-170.

Caamaño, D., P. Goodwin, and J. M. Buffington (2012), Flow structure through pool-riffle sequences and a conceptual model for their sustainability in gravel-bed rivers, *River Research and Applications*, *28*, 377-389.

Cardenas, M. B., and J. L. Wilson (2007), Effects of current-bed form induced fluid flow on thermal regime of sediments, *Water Resources Research*, *43*, W08431.

Claxton, A. J., P. D. Bates, and H. L. Cloke (2003), Mixing of hillslope, river, and alluvial ground waters in lowland floodplains, *Ground Water*, *41*, 926-936.

Constantz, J., A. E. Stewart, R. Niswonger, and L. Sarma (2002), Analysis of temperature profiles for investigating stream losses beneath ephemeral channels, *Water Resources Research*, *38*, 1316.

Cooper, A. C. (1965), The effect of transported stream sediments on the survival of sockeye and pink salmon eggs and alevin, International Pacific Salmon Fisheries Commission, New Westminster, B.C., Canada.

Cuthbert, M. O., and R. Mackay (2013), Impacts of nonuniform flow on estimates of vertical streambed flux, *Water Resources Research*, *49*, 19–28.

DeVries, P. (1997), Riverine salmonid egg burial depths: a review of published data and implications for scour studies, *Canadian Journal of Fisheries and Aquatic Sciences*, *54*, 1685-1698.

Fanelli, R. M., and L. Lautz (2008), Water, heat and solute fluxes through the hyporheic zone of small dams, *Ground Water*, *46*, 671-687.

Ferguson, G., and V. Bense (2011), Uncertainty in 1D heat-flow analysis to estimate groundwater discharge to a stream, *Ground Water*, *49*, 336-347.

Geist, D. R., and D. D. Dauble (1998), Redd site selection and spawning habitat use by fall Chinook salmon: the importance of geomorphic features in large rivers, *Environmental management*, *22*, 655-669.

Geist, D. R., T. P. Hanrahan, E. V. Arntzen, G. A. McMicheal, C. J. Murray, and Y.-J. Chien (2002), Physicochemical characteristics of the hyporheic zone affect redd site selection by chum salmon and fall Chinook salmon in the Columbia River, *North American Journal of Fisheries Management*, *22*, 1077-1085.

Gordon, R. P., L. Lautz, M. A. Briggs, and J. M. McKenzie (2012), Automated calculation of vertical pore-water flux from field temperature time series using the VFLUX method and computer program, *Journal of Hydrology*, *420-421*, 142-158.

Goto, S., M. Yamano, and M. Kinoshita (2005), Thermal response of sediment with vertical fluid flow to periodic temperature variation at the surface, *Journal of Geophysical Research*, *110*, B01106.

Hannah, D. M., I. A. Malcolm, and C. Bradley (2009), Seasonal hyporheic temperature dynamics over riffle bedforms, *Hydrological Processes*, *23*, 2178-2194.

Harvey, J. W., and K. E. Bencala (1993), The effect of streambed topography on surface-subsurface water exchange in mountain catchments, *Water Resources Research*, *29*, 89-98.

Hatch, C., A. T. Fisher, J. S. Revenaugh, J. Constantz, and C. Ruehl (2006), Quantifying surface water–groundwater interactions using time series analysis of streambed thermal records: Method development, *Water Resources Research*, *42*, W10410.

Hatch, C., A. T. Fisher, C. Ruehl, and G. Stemler (2010), Spatial and temporal variations in streambed hydraulic conductivity quantified with time-series thermal methods, *Journal of Hydrology*, *389*, 276-288.

Isaak, D. J., R. F. Thurow, B. E. Rieman, and J. B. Dunham (2007), Chinook salmon use of spawning patches: Relative roles of habitat quality, size and connectivity, *Ecological Applications*, *17*, 352-364.

Keery, J., A. Binley, N. Crook, and J. W. N. Smith (2007), Temporal and spatial variability of groundwater–surface water fluxes: Development and application of an analytical method using temperature time series, *Journal of Hydrology*, *336*, 1-16.

Kennedy, C. D., D. P. Genereux, D. R. Corbett, and H. Mitasova (2009a), Relationships among groundwater age, denitrification, and the coupled groundwater and nitrogen fluxes through a streambed, *Water Resources Research*, *45*, W09402.

Kennedy, C. D., D. P. Genereux, D. R. Corbett, and H. Mitasova (2009b), Spatial and temporal dynamics of coupled groundwater and nitrogen fluxes through a streambed in an agricultural watershed, *Water Resources Research*, *45*, W09401.

Krause, S., D. M. Hannah, and T. Blume (2011), Interstitial pore-water temperature dynamics across a pool-riffle-pool sequence, *Ecohydrology*, *4*, 549-563.

Lapham, W. W. (1989), Use of temperature profiles beneath streams to determine rates of vertical ground-water flow and vertical hydraulic conductivity, edited by D. o. t. Interior.

Lautz, L. (2012), Observing temporal patterns of vertical flux through streambed sediments using time-series analysis of temperature records, *Journal of Hydrology*, *464-565*, 199-215.

Lautz, L. K. (2010), Impacts of nonideal field conditions on vertical water velocity estimates from streambed temperature time series, *Water Resources Research*, *46*, W01509.

Luce, C. H., and D. G. Tarboton (2010), Evaluation of alternative formulae for calculation of surface temperature in snowmelt models using frequency analysis of temperature observations, *Hydrology and Earth System Sciences*, *14*, 535-543.

Luce, C. H., D. Tonina, F. Gariglio, and R. Applebee (2013), Solutions for the diurnally forced advection-diffusion equation to estimate bulk fluid velocity and diffusivity in streambeds from temperature time series, *Water Resources Research*, *49*, 488-506.

Malard, F., K. Tockner, M.-J. Dole-Olivier, and J. V. Ward (2002), A landscape perspective of surface–subsurface hydrological exchanges in river corridors, *Freshwater Biology*, *47*, 621-640.

Malcolm, I. A., A. F. Youngson, and C. Soulsby (2003), Survival of salmonid eggs in a degraded gravel-bed stream: effects of groundwater-surface water interactions, *River Research and Applications*, *19*, 303-316.

Marzadri, A., D. Tonina, and A. Bellin (2011), A semianalytical three-dimensional process-based model for hyporheic nitrogen dynamics in gravel bed rivers, *Water Resources Research*, *47*, W11518.

Marzadri, A., D. Tonina, and A. Bellin (2012), Morphodynamic controls on redox conditions and on nitrogen dynamics within the hyporheic zone: Application to gravel bed rivers with alternate-bar morphology, *Journal of Geophysical Research: Biogeosciences*, *117*.

Marzadri, A., D. Tonina, and A. Bellin (2013), Effects of stream morphodynamics on hyporheic zone thermal regime, *Water Resources Research*, *49*, 2287-2302.

Marzadri, A., D. Tonina, A. Bellin, G. Vignoli, and M. Tubino (2010), Effects of bar topography on hyporheic flow in gravel-bed rivers, *Water Resources Research*, *46*, W07531.

McGlynn, B. L. (2005), The role of riparian zones in steep mountain watersheds, in *Global Change and Mountain Regions: An Overview of Current Knowledge*, edited by U. M. Huber, et al., Springer, Dordrecht, Netherlands.

McKean, J. A., and D. Tonina (2013), Bed stability in unconfined gravel-bed mountain streams: With implications for salmon spawning viability in future climates, *Journal of Geophysical Research: Earth Surface*, *in press*.

Montgomery, D. R., and J. M. Buffington (1997), Channel-reach morphology in mountain drainage basins, *Geological Society of America Bulletin*, *109*, 596-611.

Naiman, R. J. (1998), Biotic stream classification, in *River Ecology and Management: Lessons from the Pacific Coastal Ecoregion*, edited by R. J. Naiman and R. E. Bilby, pp. 97-119, Springer-Verlag, New York.

Pinay, G., T. C. O'Keefe, R. T. Edwards, and R. J. Naiman (2009), Nitrate removal in the hyporheic zone of a salmon river in Alaska, *River Research and Applications*, *25*, 367-375.

Pretty, J. L., A. G. Hildrew, and M. Trimmer (2006), Nutrient dynamics in relation to surface–subsurface hydrological exchange in a groundwater fed chalk stream, *Journal of Hydrology*, *330*, 84-100.

Revsbech, N. P., J. P. Jacobsen, and L. P. Nielsen (2005), Nitrogen transformations in microenvironments of river beds and riparian zones, *Ecological Engineering*, *24*, 447-455.

Savant, A. S., D. D. Reible, and L. J. Thibodeaux (1987), Convective Transport Within Stable River Sediments, *Water Resources Research*, *23*, 1763-1768.

Schornberg, C., C. Schmidt, E. Kalbus, and J. H. Fleckenstein (2010), Simulating the effects of geologic heterogeneity and transient boundary conditions on streambed temperatures - implications for temperature-based water flux calculations, *Advances in Water Resources*, *33*, 1309-1319.

Shanafield, M., C. Hatch, and G. Pohll (2011), Uncertainty in thermal time series analysis estimates of streambed water flux, *Water Resources Research*, *47*, W03504.

Shiono, K., T. Ishigaki, Y. Muto, and H. Imamoto (1999), Bed shear stress in meandering channels for overbank flow, paper presented at IAHR Biennial Congress, Publ. on CD, Graz, Austria.

Stallman, R. W. (1965), Steady 1 – dimensional fluid flow in a semi-infinite porous medium with sinusoidal surface temperature, *Journal of Geophysical Research*, *70*, 282102827.

Stanford, J. A., and J. V. Ward (1988), The hyporheic habitat of river ecosystems, *Nature*, *335*, 64-65.

Stanford, J. A., and J. V. Ward (1993), An ecosystem perspective of alluvial rivers: connectivity and the hyporheic corridor, *Journal of the North American Benthological Society*, *12*, 48-60.

Storey, R. G., K. W. F. Howard, and D. D. Williams (2003), Factor controlling riffle-scale hyporheic exchange flows and their seasonal changes in gaining stream: a three-dimensional groundwater model, *Water Resources Research*, *39*, 17, doi:10.1029/2002WR001367.

Storey, R. G., D. D. Williams, and R. R. Fulthorpe (2004), Nitrogen processing in the hyporheic zone of a pastoral stream, *Biogeochemestry*, *69*, 285-313.

Strahler, A. N. (1952), Hypsometric (area-altitude) analysis of erosional topography, *Bulletin of the Geological Society of America*, *63*, 1117 - 1142.

Stuart, T. A. (1953), Water currents through permeable gravel and their significance to spawning salmonids, etc., *Nature*, *172*, 407-408.

Swanson, T. E., and B. M. Cardenas (2010), Diel heat transport within the hyporheic zone of a pool-riffle-pool sequence of a losing stream and evaluation of models for fluid flux estimation using heat, *Limnology and Oceanography*, *55*, 1741-1754.

Taylor, C. J., D. J. Pedregal, P. C. Young, and W. Tych (2007), Environmental time series analysis and forecasting with the Captain toolbox, *Environmental Modelling & Software*, *22*, 797-814.

Tonina, D., and J. M. Buffington (2007), Hyporheic exchange in gravel bed rivers with pool-riffle morphology: Laboratory experiments and three-dimensional modeling, *Water Resources Research*, *43*.

Tonina, D., and J. M. Buffington (2009a), Hyporheic exchange in mountain rivers I: Mechanics and environmental effects *Geography Compass*, *3*, 1063 - 1086.

Tonina, D., and J. M. Buffington (2009b), A three-dimensional model for analyzing the effects of salmon redds on hyporheic exchange and egg pocket habitat, *Canadian Journal of Fisheries and Aquatic Sciences*, *66*, 2157-2173.

Tonina, D., and J. M. Buffington (2011), Effects of stream discharge, alluvial depth and bar amplitude on hyporheic flow in pool-riffle channels, *Water Resources Research*, *47*, W08508.

Tonina, D., and J. A. McKean (2010), Climate change impact on salmonid spawning in low-land streams in Central Idaho, USA, paper presented at 9th International Conference on Hydroinformatics, Chemical Industry Press, Tianjin, China.

Tonina, D., J. A. McKean, C. Tang, and P. Goodwin (2011), New tools for aquatic habitat modeling, paper presented at 34th IAHR World Congress - Balance and Uncertainty

33rd Hydrology and Water Resources Symposium

10th Hydraulics Conference, IAHR, Brisbane, Australia.

Triska, F. J., V. C. Kennedy, R. J. Avanzino, G. W. Zellweger, and K. E. Bencala (1989), Retention and transport of nutrients in a third-order stream in Northwestern California: Hyporheic processes, *Ecology*, *70*, 1893-1905.

Van Grinsven, M., A. Mayer, and C. Huckins (2012), Estimation of streambed groundwater fluxes associated with coaster brook trout spawning habitat, *Ground Water*, *50*, 432-441.

Vannote, R. L., W. G. Minshall, K. W. Cummins, J. R. Sedell, and C. E. Cushing (1980), The River Continuum Concept, *Canadian Journal of Fisheries and Aquatic Sciences*, *37*, 130-137.

Vogt, T., P. Schneider, L. Hahn-Woernle, and O. A. Cirpka (2010), Estimation of seepage rates in a losing stream by means of fiber-optic high-resolution vertical temperature profiling, *Journal of Hydrology*, *380*, 154-164.

Whiting, P. J., and M. Pomeranets (1997), A numerical study of bank storage and its contribution to streamflow, *Journal of Hydrology*, *202*, 121-136.

Winter, T. C., J. W. Harvey, O. L. Franke, and W. M. Alley (1998), Ground water and surface water a single resource, Circular, U.S. Geological Survey.

Wroblicky, G. J., M. E. Campana, M. H. Valett, and C. N. Dahm (1998), Seasonal variation in surface-subsurface water exchange and lateral hyporheic area of two stream-aquifer systems, *Water Resources Research*, *34*, 317-328.

Zarnetske, J. P., R. Haggerty, S. M. Wondzell, and M. A. Baker (2011), Dynamics of nitrate production and removal as a function of residence time in the hyporheic zone, *Journal of Geophysical Research*, *116*, G01025.

	Location Code								
	Left Upstream Pool (LUP)	**Central Upstream Pool (CUP)**	**Right Upstream Pool (RUP)**	**Upstream Riffle (UR)**	**Left Riffle (LR)**	**Central Riffle (CR)**	**Right Riffle (RR)**	**Downstream Riffle (DR)**	**Downstream Pool (DP)**
n	8[a,b]	13[b]	10[b,c]	13	10[b,c]	8[c]	13	13	7[c]
q_{mean} (cm day^{-1})	59.0	50.7	-17.6	31.1	35.8	18.6	-24.3	30.3	10.5
q_{median} (cm day^{-1})	64.0	59.0	-8.7	32.2	58.0	19.4	-25.6	26.1	9.0
variance, σ^2	99.7	271.8	529.7	37.7	863.1	28.9	63.5	350.2	24.3
std dev, σ	10.0	16.5	23.0	6.1	29.4	5.4	8.0	18.7	4.9
min	37.0	19.0	-79.0	12.6	-7.9	9.7	-37.9	10.6	5.9
max	64.0	68.0	6.0	39.0	58.0	28.3	0.1	66.7	19.4

[a] thermal profiles outside of acceptable calculation limits (no flux calculated)

[b] thermal profiles leading to non-unique solution (seepage flux set to minimum UW or DW velocity to fit profile)

[c] calculated seepage flux less than accepted minimum value from equation (5) (no flux reported)

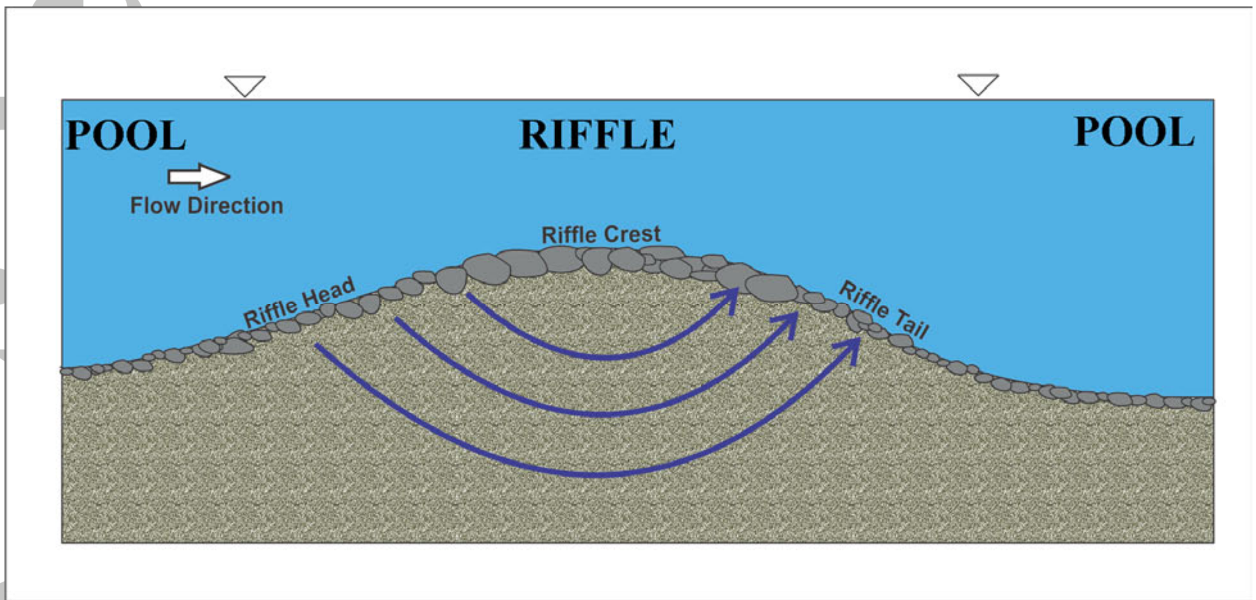

Figure 1. Conceptualized longitudinal seepage flux pattern for a pool-riffle-pool morphological feature. Hydraulic gradients resulting from streambed topography drive downwelling and upwelling flows across the riffle.

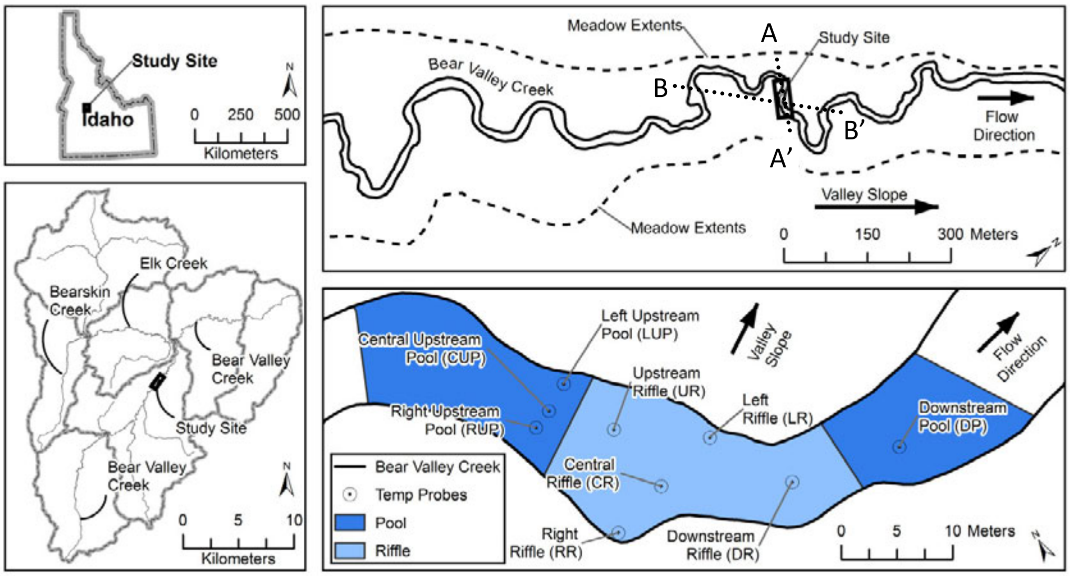

Figure 2: Location map, area map, and site location map of Bear Valley Creek study site. The site location map shows the spatial arrangement of temperature measurement probes and the location ID used for each probe. Sections A-A' and B-B' in the upper right panel are theoretical profiles, representing the longitudinal channel gradient (A-A') and down valley gradient (B-B'), used to interpret system behavior. The theoretical profiles correspond to the sections presented in Figure 14.

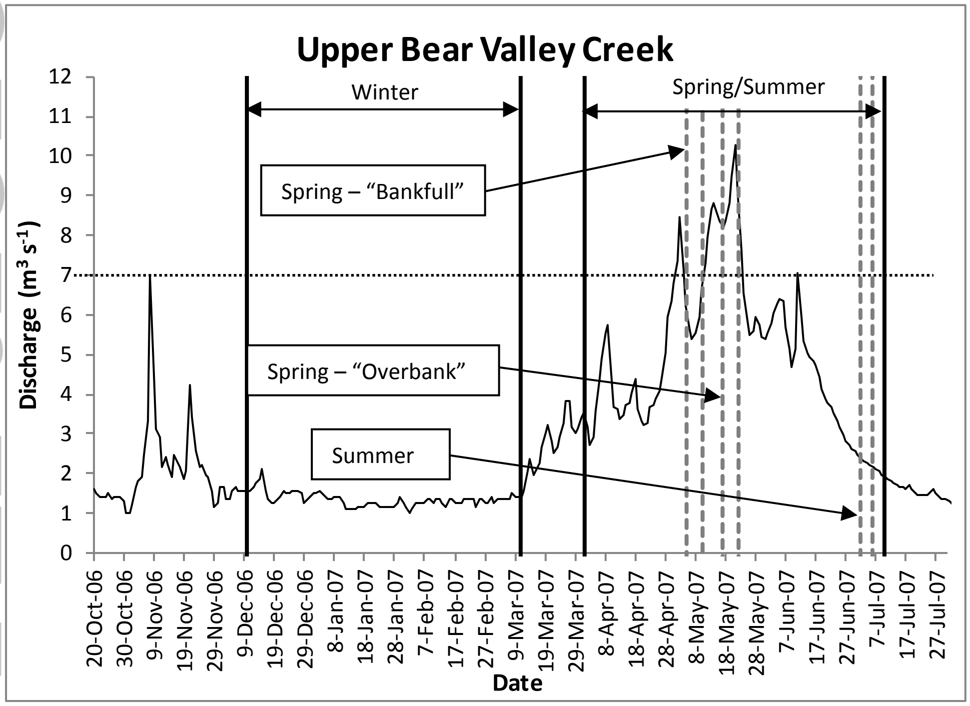

Figure 3: Reconstructed Bear Valley Creek hydrograph. Approximate bankfull flow is shown by the horizontal dashed line. Time windows show periods selected for more detailed analysis.

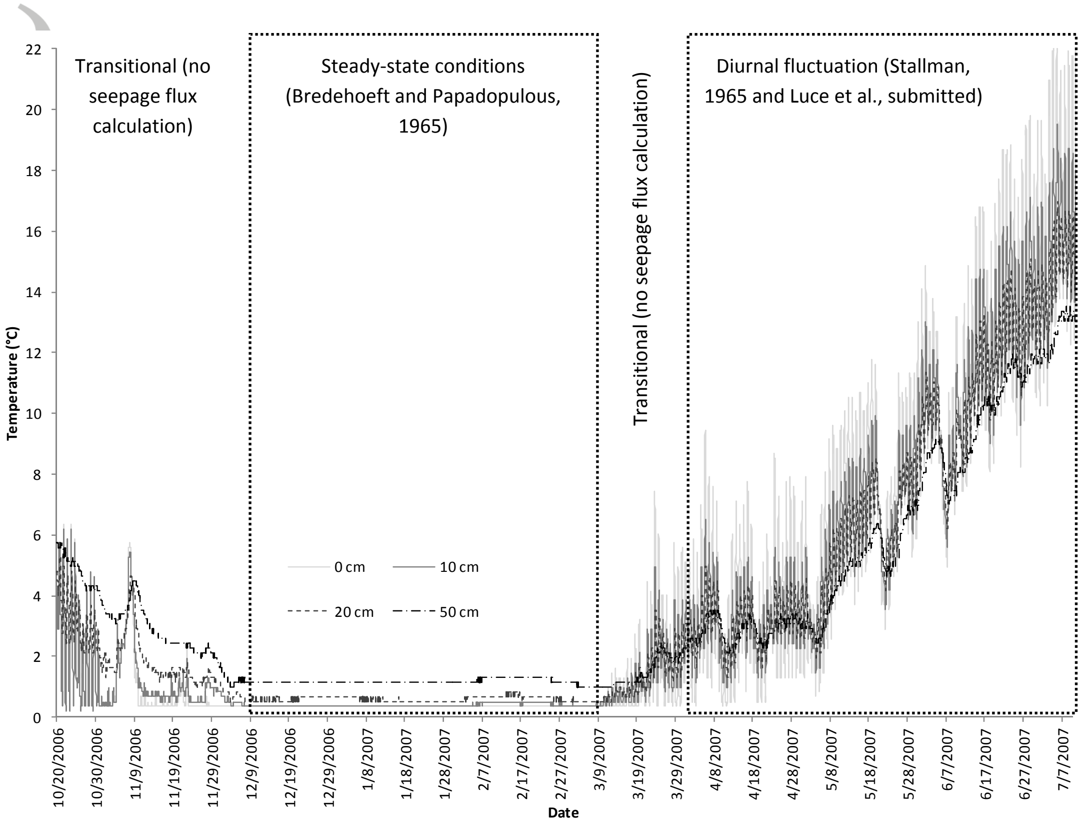

Figure 4: Measured temperature profiles at the central riffle (CR) location. Winter temperature profiles are characterized by little to no temperature fluctuation for the surface water or at depth within the streambed (approximating steady state conditions). Spring and summer temperatures are characterized by diurnally fluctuating surface water and streambed temperatures. Temperatures from 16 October 2006 – 10 December 2006 and 11 March 2007 – 30 March 2007 were not readily categorized as steady state or diurnally fluctuating (without preferential flow for the fall season) and so were not used for calculating seepage flux.

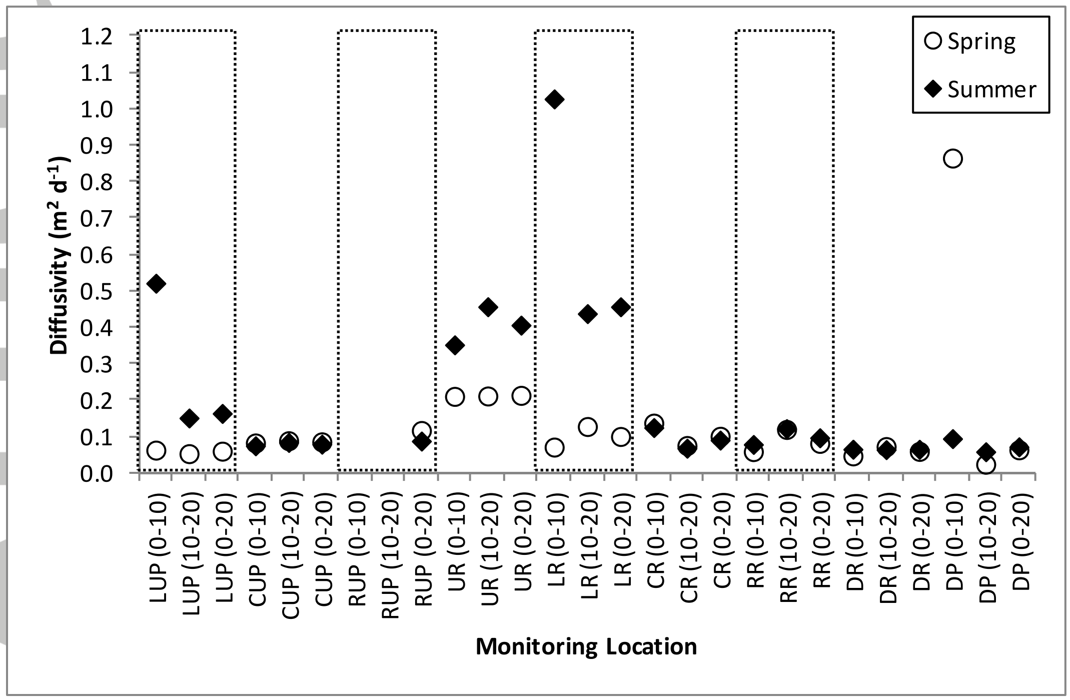

Figure 5: Calculated thermal diffusivity values for spring (08 May 2007 – 12 May 2007) and summer (02 Jul 2007 – 06 Jul 2007) time periods. Dashed outlines highlight the temperature monitoring locations near the edges of the channel. Note that the 10-cm sensor at the RUP location failed.

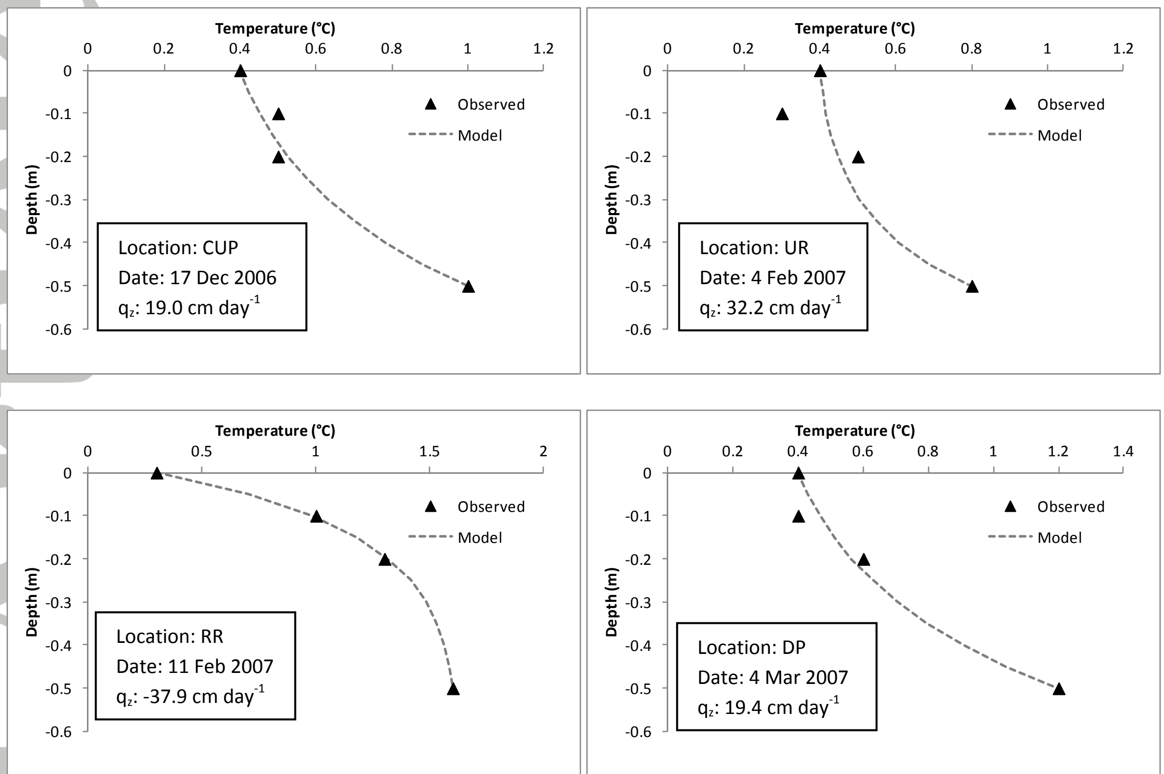

Figure 6: Example weekly thermal profile fit with streambed seepage flux calculated from Bredehoeft and Papadopulos [1965] method. Dates correspond to the beginning of the period where streambed seepage flux was calculated. Negative velocities represent upwelling conditions and positive velocities represent downwelling conditions.

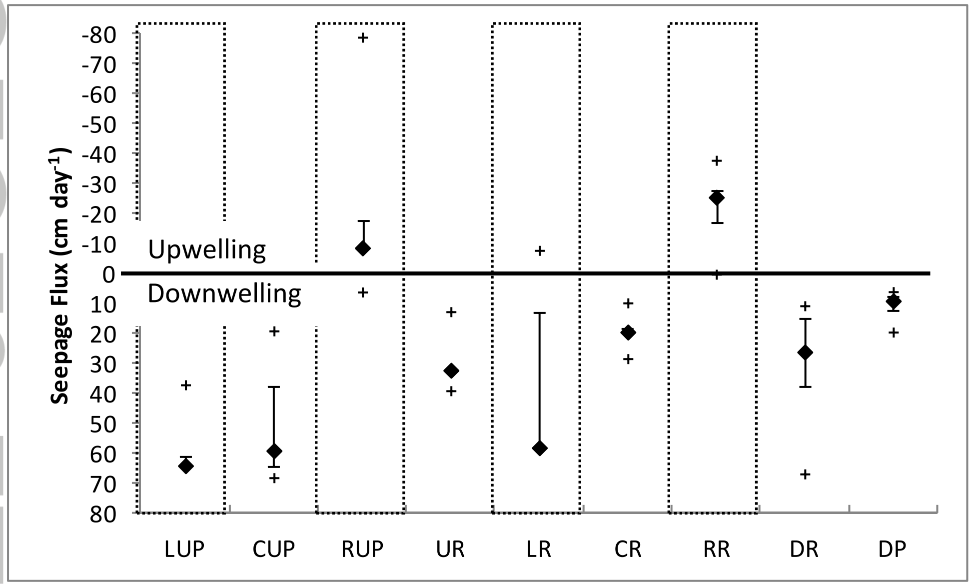

Figure 7: Median weekly streambed seepage flux from 10 December 2006 through 10 March 2007. Bars indicate the 25th and 75th percentile seepage flux values. Crosses indicate the maximum and minimum calculated seepage fluxes. Dashed outlines highlight the temperature monitoring locations near the edges of the channel.

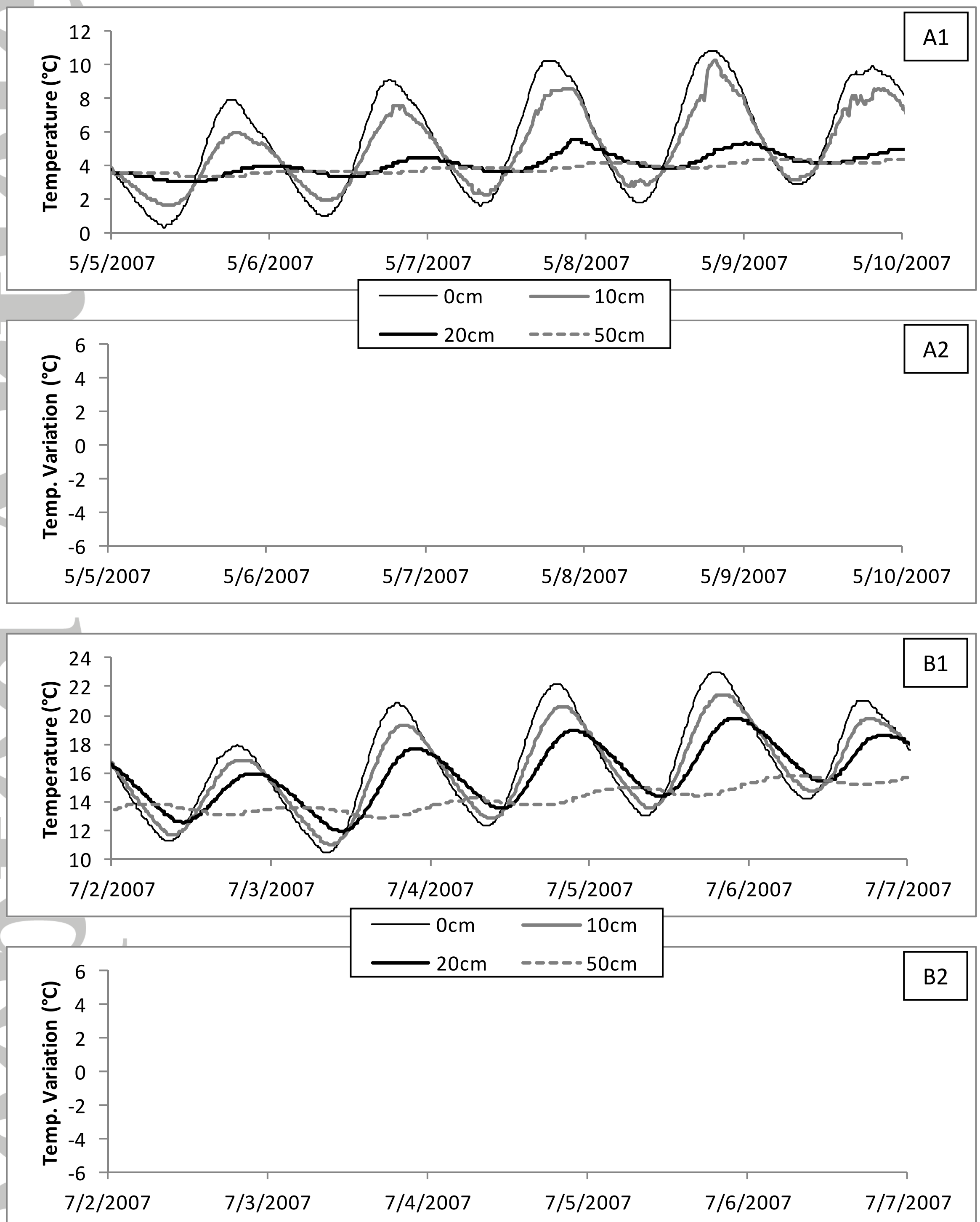

Figure 8: Raw thermal time series for A1) Spring - Bankfull (DP location) and B1) Summer – Low Flow (LUP location). A2 and B2 represent the sinusoidal component (centered around a

mean of zero) of each time series with a diurnal period, obtained using DHR. Note that the axes used between plots are not identical.

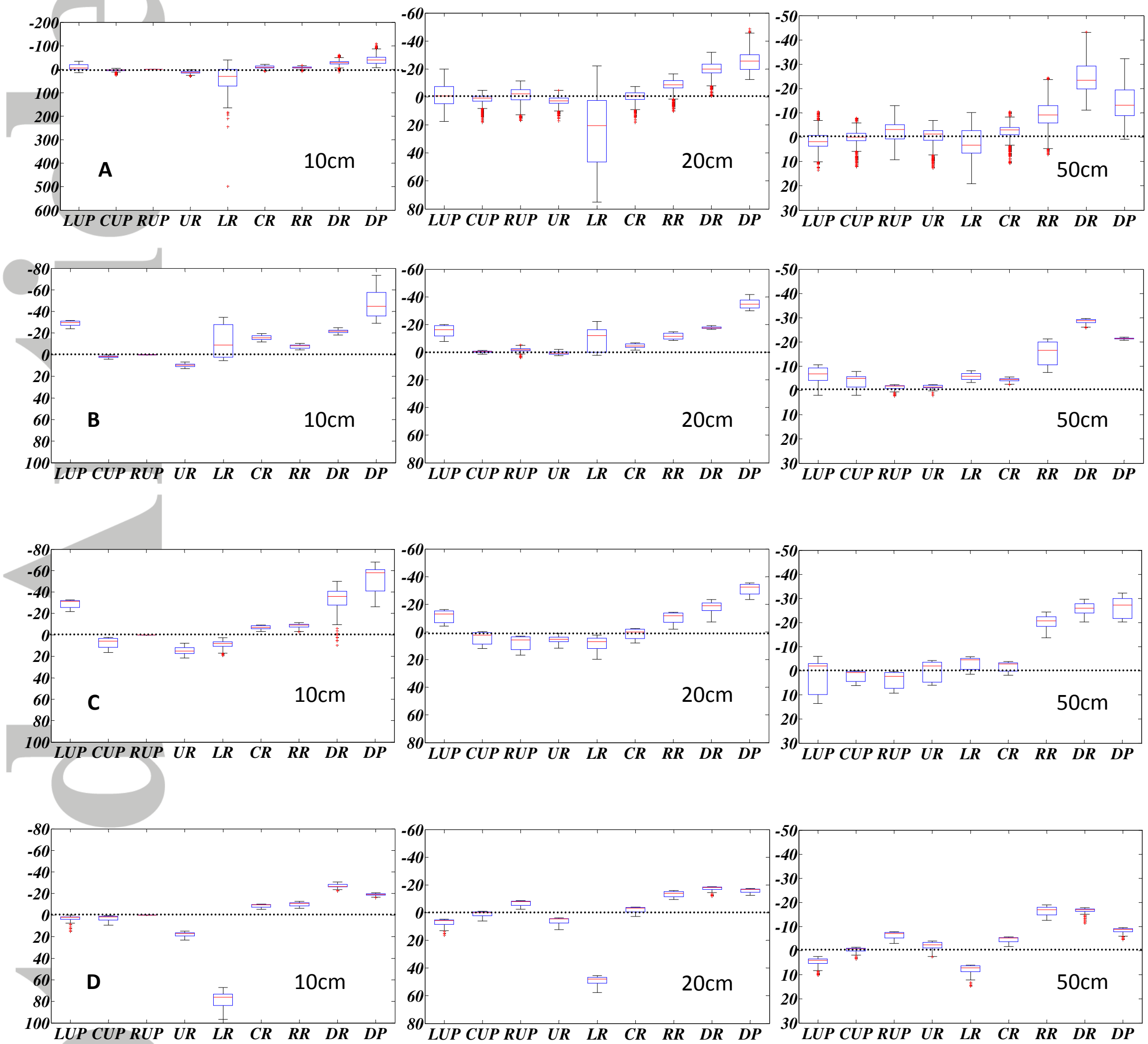

Figure 9: Box-and-whiskers plot of seepage flux at depths of 10, 20 and 50 cm. The boxes indicate the 25th and 75th percentile seepage flux values. Whiskers indicate the 10th and 90th percentile seepage fluxes, and outliers are identified with a cross. Plots are for the A) entire period analyzed (03 Apr 2007 – 08 Jul 2007) and for three representative five day windows that correspond to B) "Spring – Bankfull" (05 May 2007 – 09 May 2007), C) "Spring – Overbank" (17 May 2007 – 21 May 2007) and D) "Summer – Low Flow" (02 Jul 2007 – 06 Jul 2007). Note that the 10-cm sensor at the RUP location failed. All seepage flux magnitudes are in cm day^{-1}.

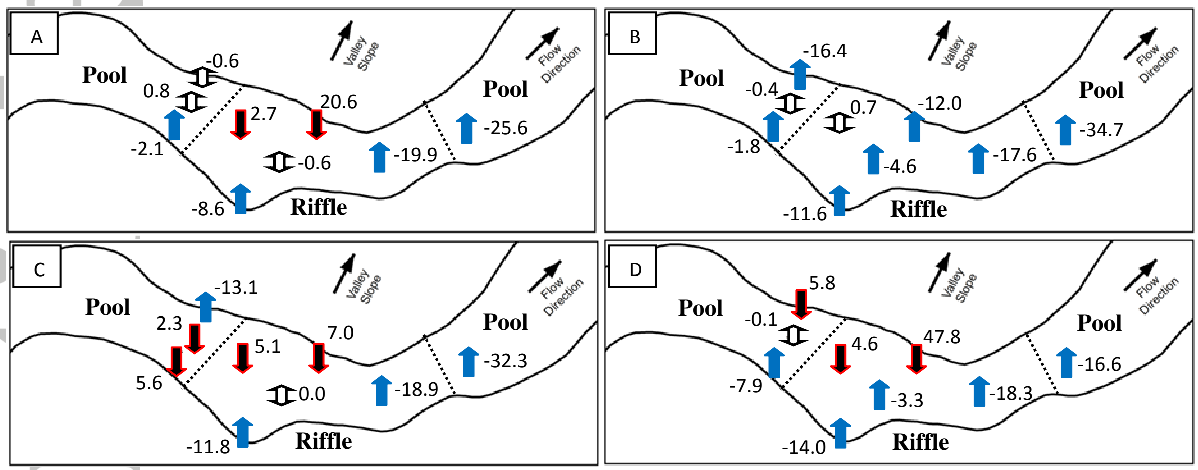

Figure 10. Median seepage flux velocities at 20-cm depth for A) entire period, B) “Spring – Bankfull”, C) “Spring – Overbank” and D) “Summer – Low Flow”. Downward, blue arrows indicate downwelling seepage fluxes and upward, red arrows indicate upwelling seepage fluxes. The blue and red signify that upwelling water is typically cooler than downwelling water during these time windows. Seepage fluxes between -1 and 1 cm day^{-1} are represented by bi-directional arrows. Dashed lines represent the transition between pool and riffle features. All seepage flux magnitudes are in cm day^{-1}.

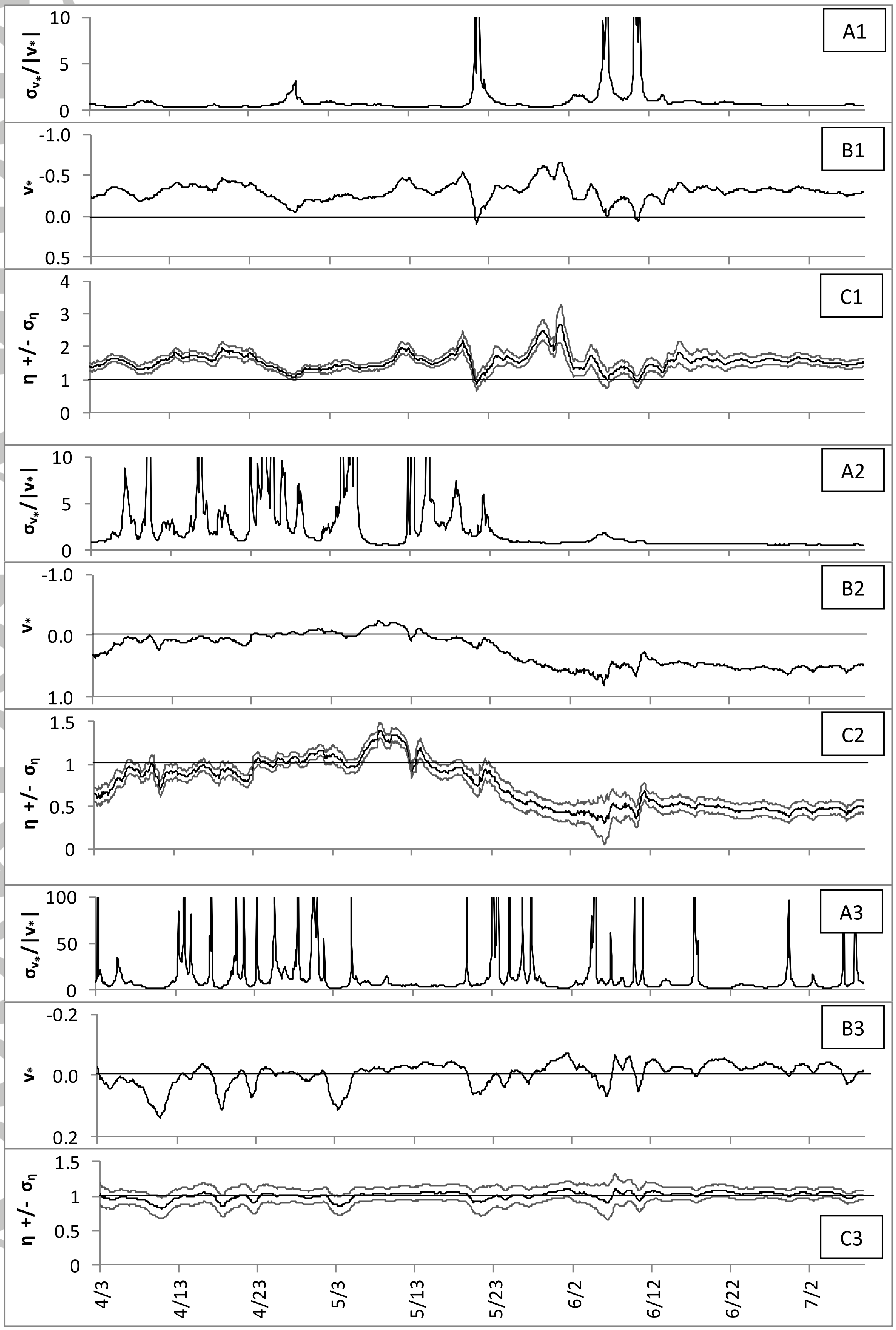
A1
σv*/|v*|
0
5
10
B1
v*
-1.0
-0.5
0.0
0.5
C1
η +/- ση
0
1
2
3
4
A2
σv*/|v*|
0
5
10
B2
v*
-1.0
0.0
1.0
C2
η +/- ση
0
0.5
1
1.5
A3
σv*/|v*|
0
50
100
B3
v*
-0.2
0.0
0.2
C3
η +/- ση
0
0.5
1
1.5
4/3
4/13
4/23
5/3
5/13
5/23
6/2
6/12
6/22
7/2

Figure 11: A) coefficient of variation for v*, B) v* and C) η +/- $\sigma\eta$ plots for the DR sensor at a depth of 10 cm (denoted with a “1”), LR sensor at a depth of 20 cm (denoted with a “2”), and UR sensor at a depth of 50 cm (denoted with a “3”). Horizontal lines represent upwelling/downwelling transitions. Note that the axes used between plots are not identical.

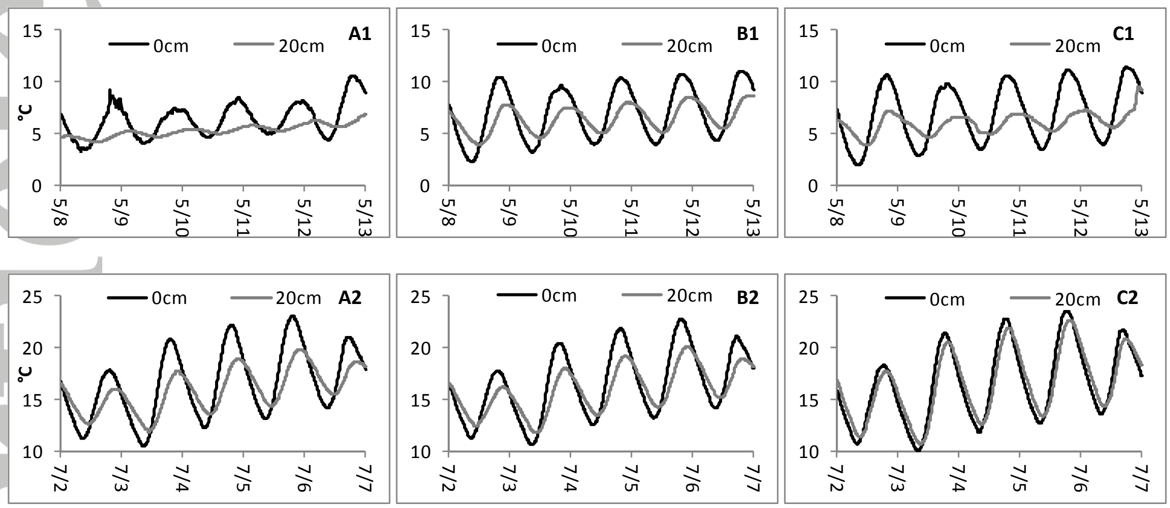

Figure 12: Raw temperature profiles for A1) LUP (08 May 2007 – 12 May 2007), A2) LUP (02 Jul 2007 – 07 Jul 2007), B1) UR (08 May 2007 – 12 May 2007), B2) UR (02 Jul 2007 – 06 Jul 2007), C1) LR (08 May 2007 – 12 May 2007) and C2) LR (02 Jul 2007 – 06 Jul 2007). Only the 0 and 20 cm temperature traces are shown for clarity. Note that spring (A1, B1, C1) profiles are more indicative of upwelling conditions while summer (A2, B2, C2) profiles are more indicative of downwelling conditions.

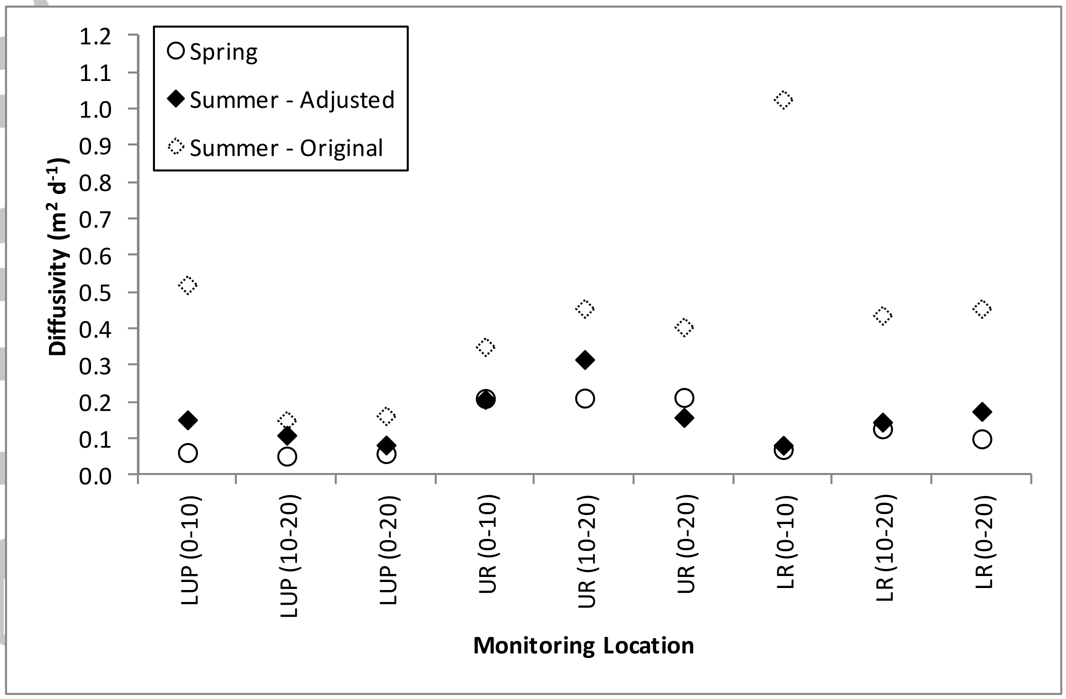

Figure 13: Adjustments to estimated thermal diffusivity values during the summer time window (02 Jul 2007 – 06 Jul 2007) based on adjusting phase angle values. Phase angle values from DHR were compared to visual determination of time shifts during periods when high frequency components of temperature signals led to small estimates of the phase angle between surface and depth sensors.

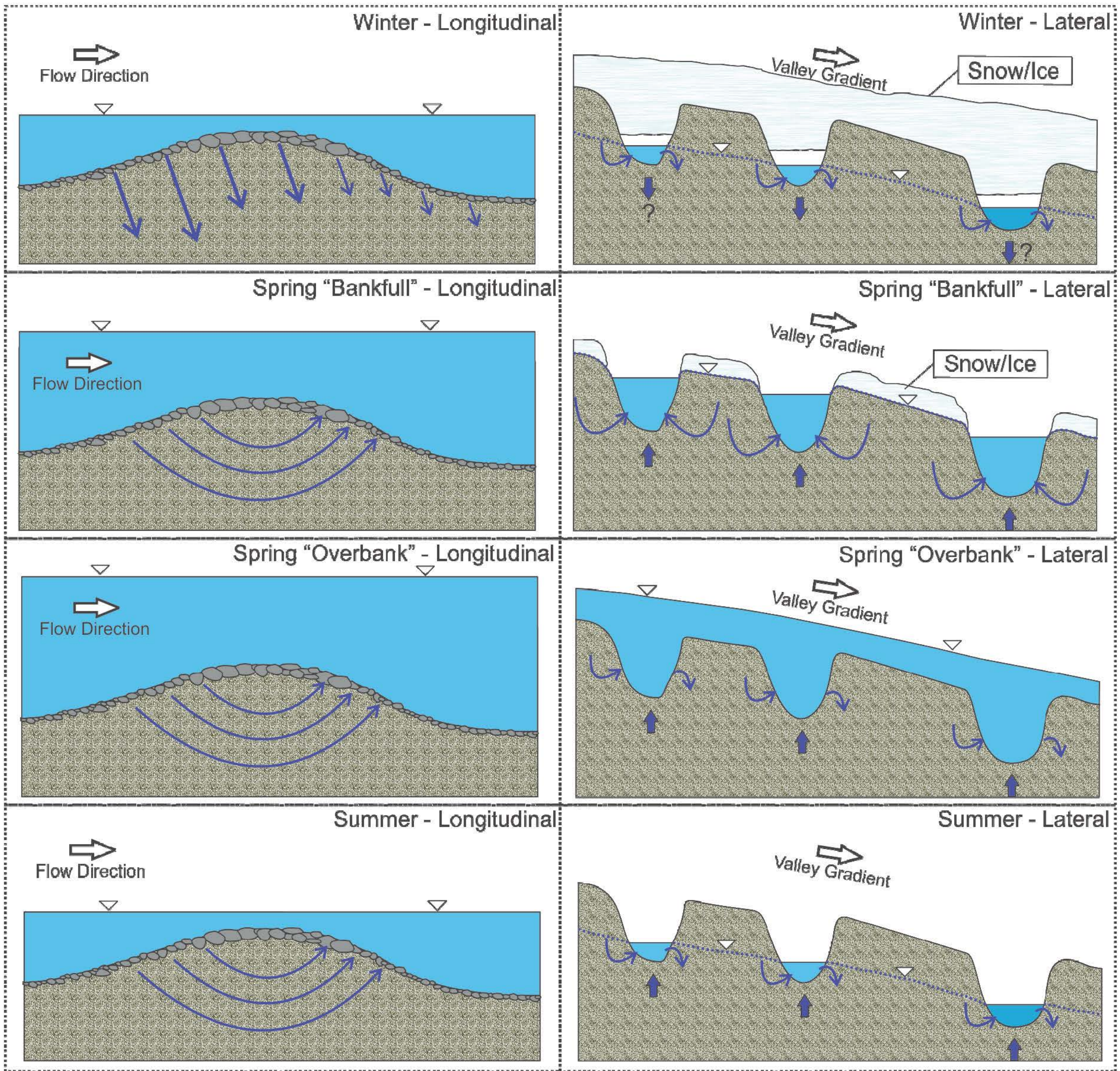

Figure 14: Conceptual model of longitudinal and cross-channel seepage flux characteristics during the winter, spring “bankfull”, spring “overbank” and summer seasons based on interpretations of flux predictions from all sensors at the study site. Note that winter longitudinal fluxes represent predominantly losing conditions. For cross-channel plots arrows below the channel indicate the general 50 cm flux direction.